



HAL
open science

The influence of self-assembled monolayers on the practical adhesion of a cataphoretic paint

Agathe Rougier, Maëlen Aufray, Jean-Marie Melot, Francis Touyeras, Xavier Roizard, Xavier Gabrion, Jean-Yves Hihn, Fabrice Lallemand

► To cite this version:

Agathe Rougier, Maëlen Aufray, Jean-Marie Melot, Francis Touyeras, Xavier Roizard, et al.. The influence of self-assembled monolayers on the practical adhesion of a cataphoretic paint. *Journal of Adhesion Science and Technology*, 2023, 37, 10.1080/01694243.2023.2230648 . hal-04224566

HAL Id: hal-04224566

<https://hal.science/hal-04224566>

Submitted on 2 Oct 2023

HAL is a multi-disciplinary open access archive for the deposit and dissemination of scientific research documents, whether they are published or not. The documents may come from teaching and research institutions in France or abroad, or from public or private research centers.

L'archive ouverte pluridisciplinaire **HAL**, est destinée au dépôt et à la diffusion de documents scientifiques de niveau recherche, publiés ou non, émanant des établissements d'enseignement et de recherche français ou étrangers, des laboratoires publics ou privés.

32

33 Word count: 9790 words

34

35

36 ABSTRACT

37 The objective of this study is to replace steel-phosphating treatments with self-
38 assembled monolayers (SAMs), in this case, of phosphonic acids. Two industrial
39 applications are targeted:

- 40 - Obtaining an adhesion primer between steel and paint or lubricating stainless
41 steel for mechanical applications, such as stamping.
- 42 - Research has been conducted using alkyl phosphonic acids. The carbon chain
43 length and terminal function are changed to obtain the best properties
44 depending on the application.

45 Keywords: Self-assembled monolayers, adhesion, primer, stainless steel

46

47

48 I. Introduction

49

50 Since the 1990s, regulations relating to knowledge of chemicals and assessment of their risks
51 have led industries to innovate and develop increasingly environmentally friendly products. The
52 steel-phosphating process, initiated in 1907 with the Coslett patent [1], is a surface treatment
53 with several disadvantages: the production of metallic waste necessitates several rinses with
54 subsequent treatments over time, requiring staff to follow these treatments. The presence of
55 nitrites, nitrates, and concentrated acids in the bath requires hazardous manipulations [2].
56 Moreover, the miniaturization of currently manufactured products to achieve a thickness of
57 approximately 10 to 30 μm is also problematic. A phosphatation replacement should ensure
58 anti-corrosion, adhesion to paint, and anti-wear properties.

59 Thus, in recent years, research has been conducted on alternatives to phosphate coatings.
60 Different options are currently available on the market or described in the literature. These
61 include phosphating with a modified composition [3], sol-gels [4-20], and very thin coatings
62 such as self-assembled monolayers (SAMs).

63 As phosphating is used for not only its adhesion and anti-corrosion properties but also its anti-
64 wear properties, alternatives exist for applications such as cold forming and lubrication. In
65 recent years, research has been conducted on dry lubricants to solve the problems of waste and
66 cleaning after lubrication, which are costly for industries. These dry lubricants are manufactured
67 with self-assembled monolayers. This nanometer-scale deposition is obtained by immersing a
68 metal substrate in a modification solution containing active molecules at a low concentration
69 [21-22]. These molecules are grafted onto the surface oxides by chemisorption [23], forming a
70 monolayer with different properties depending on the molecules used. Since the early 2000s,
71 SAMs have been increasingly used for their ease of manipulation, reproducibility, stability [24],
72 and versatility [25]. Research has focused on alkylphosphonic acids to continue using an
73 environmentally friendly process [26-29]. Notably, studies performed on copper showed
74 improved tribological [30] and anti-corrosion properties [31-32]. A few years later, a new
75 process for surface functionalization without surface preparation was patented and applied in
76 industry [33].

77 Research has been conducted using phosphonic acids to obtain adherence properties on copper
78 with a carboxylic termination [34-35]. This study was conducted based on this research. In this
79 research, practical adhesion (*i.e.* adherence) was studied with two adherence tests: the single
80 lap joint (SLJ) (AFNOR, NF EN 2243-1) and three-point bending (AFNOR, ISO 14679: 1997)
81 tests. An epoxy-based glue, Araldite 103-1, with a hardener, HY 991, was used to closely align
82 with the industrial conditions of cathoretic painting, which also has an epoxy function.
83 Phosphate coating is replaced with SAMs, where the carbon chain length and the terminal

84 function have been modified to obtain the best properties from the phosphating treatment and
85 the best fracture resistance.

86 **II. Materials and methods**

87 ***1. Material and sample preparation***

88 a. *Substrates*

89 The metallic substrate used was a plate of austenitic AISI 304 stainless steel (304SS) with a
90 thickness of 0.8 mm for three-point bending tests. The 304SS substrate had a thickness of
91 0.5 ± 0.05 mm for the SLJ and pull-off test. The chemical composition and roughness
92 parameters are shown in Table 1.

93 b. *Synthesis of alkylphosphonic acids*

94 All alkylphosphonic acids were synthesized in the laboratory. All molecules are represented in
95 Figure 1 and were analyzed by ^1H and ^{31}P Nuclear magnetic resonance (NMR). Their purity
96 exceeded 95%.

97 **Other syntheses are described (see below).**

98 **11-phosphoundecanoic acid (C10COOH) synthesis:**

99 Although commercially available, this product can be efficiently synthesized in multigram
100 quantities from cheap materials. Commercial 11-bromoundecanoic acid from Sigma Aldrich
101 was esterified with excess absolute ethanol in the presence of 96% sulphuric acid for 24 h. After
102 cooling, the solution was neutralized with solid sodium hydrogen carbonate and concentrated
103 *in vacuo*. The residue was dissolved in ether/water. The ethereal phase was washed with
104 saturated sodium hydrogen carbonate and dried. Evaporation of the solvent afforded ethyl 11-
105 bromoundecanoate, which was sufficiently pure for the following steps. The previous ester was

106 heated to 190°C and excess triethylphosphite (1.75–2.0 equivalents) added dropwise by stirring.
107 Bromoethane was continuously distilled as formed (35°C–40°C/760 mm Hg). The temperature
108 was raised to 210°C–215°C until no more bromoethane was extracted. A vacuum (20–50 mm
109 Hg) was progressively established with caution: excess triethylphosphite was distilled with an
110 undesirable contaminant (diethyl ethylphosphonate). The mixture, containing mainly the
111 triethyl ester of 11-phosphonoundecanoic acid, was cooled to room temperature; 12 M aqueous
112 hydrochloric acid was added and the mixture gently boiled with efficient stirring for 24 h
113 (85°C–90°C). On cooling to room temperature by stirring, crude 11-phosphonoundecanoic acid
114 was separated into thick plates, filtered, and washed with water. Recrystallization from acetic
115 acid afforded pure 11-phosphonoundecanoic acid as a white powder or off-white needles. The
116 overall yield was 75% with a melting point of 175°C–177°C.

117 **1,12-dodecanediphosphonic acid (-C12 (2P)-) synthesis:**

118 According to the work of S. Frey *and al.* [61], diethyl 1,12-dodecanediphosphonate was
119 synthesized from 1,12-dibromododecane (Alfa Aesar) and a sixfold molar excess of
120 triethylphosphite (Alfa Aesar) at 200°C before being hydrolyzed by refluxing from
121 concentrated 12 M aqueous HCl for 24 h. The thick diacid, which precipitated readily in the
122 reaction mixture, was filtered, washed free of strong acid with distilled water, and dried in air.
123 It was purified by recrystallization from an acetic acid/DMSO mixture. The overall yield
124 obtained was 65% with a melting point of 175°C–179°C.

125 **10-undecenylphosphonic acid (C9CH=CH2) synthesis:**

126 Bromoethane was formed by distilling, while 11-bromo-undec-1-ene (Sigma Aldrich) mixed
127 with a threefold molar excess of triethylphosphite (Alfa Aesar) was heated to 200°C. After the
128 reaction, excess phosphite and diethyl ethylphosphonate was distilled off (P = 40–50 mm Hg),
129 leaving diethyl undecenylphosphonate as an oil in almost quantitative yield; 15 g of the

130 preceding phosphonate was dissolved in 70 mL of dichloromethane and cooled in an ice bath,
131 while 20 mL of bromotrimethylsilane was added in four portions. No exothermic phenomena
132 were observed. After standing at 0°C for 30 min, the reaction was left at room temperature
133 overnight. Evaporation of the solvent produced a relatively mobile oil. Methanol (100 mL) and
134 water (5 mL) were then added and the mixture left for 24 h. After evaporation of the solvent,
135 the oily residue crystallized in ice. It was then recrystallized from heptane to give slightly gray
136 needles. The overall yield obtained is 41% with a melting point of 80°C–84°C.

137 **1,5-phosphonopentadecanoic acid (C14COOH) synthesis:**

138 The 1,5-bromoundecanoic acid was prepared from pentadecanolide (Sigma Aldrich) in a 90%
139 yield according to [61]; 15-phosphonopentadecanoic acid was then obtained as a white powder,
140 following method A. The melting point obtained was 118°C–121°C.

141 Previous research has described the syntheses of several alkylphosphonic acids, such as
142 butanephosphonic acid (C4P) [36], dodecanephosphonic acid (C12P) [32], and
143 hexadecanephosphonic acid (C16P) [36].

144 c. *Surface preparation*

145 Pretreatment of samples

146 The 304SS was immersed by stirring in an alkaline degreasing bath (Presol 7060, Coventya,
147 France) for 2 min at 60°C. The substrate was then rinsed with distilled water and 96% ethanol.
148 The 304SS was sonicated in 96% ethanol for 10 min before being rinsed with 96% ethanol and
149 distilled water. Finally, samples were dried with pressurized air.

150 Grafting preparation

151 The substrate was immersed in an alkylphosphonic acid ethanolic modification solution for 8 h
152 to ensure the most reproducible results with good organization of SAMs on the surface (Table
153 2) [36-37]. In some cases, it was then rinsed with 96% ethanol and distilled water. Finally, all
154 the samples were dried in an oven for 30 min at 30°C.

155 d. *Glue and bonding thermal curing*

156 Grafted samples were adhesively bonded by applying a mixture of an epoxy prepolymer and an
157 amine curing agent. The epoxy prepolymer is Araldite 103-1, while the hardener is HY 991
158 (Huntsman, USA). After bonding, samples were kept at room temperature for 3 hours. They
159 were then heated in an oven for 1 hour at 150°C before cooling to room temperature for 1 hour.

160 **2. Adherence tests**

161 Adherence measurements were conducted with the SLJ and the three-point bending tests. SLJ
162 results are usually reported as tension (MPa), while three-point bending test results are reported
163 as force (N). In this document, all results are expressed as stress.

164 Single lap joint test (AFNOR, NF EN 2243-1)

165 The SLJ is a test designed for the initiation and propagation of fractures. The 304SS bare
166 specimens used as substrates were milled for reuse after each test. First, a two-step surface
167 preparation was conducted, followed by a surface modification treatment. In a second step, the
168 specimens were placed in a special set-up allowing two substrates to be aligned, with the same
169 adhesive joints. A syringe was used to apply 0.06 mL glue. A 3 kg weight was added to the
170 specimens to ensure intimate contact between the surface and adhesive. The adhesive joint then
171 complied with the bonding protocol indicated above. A series of five adhesive joints was
172 prepared and tested for each configuration.

173 The tests were conducted on an MTS (USA) Criterion 45 machine with a 100 kN load cell at
174 room temperature. The crosshead displacement speed was 1 mm/min. Specimen dimensions
175 are described in Figure 2 (left). The maximum force (F_{\max}) was considered as the load at
176 breaking point, while the ultimate load was divided by the overlap to evaluate the lap shear
177 strength (σ_{\max} in MPa).

178 b. *Three-point bending test (AFNOR, ISO 14679: 1997)*

179 Plates of 304SS were used to perform the three-point bending test. First, the plates complied
180 with the surface preparation protocol before undergoing surface modifications. In a second step,
181 Araldite 103-1 with hardener HY991 was applied to the cut ($10.0 \pm 0.1 \text{ mm} \times 50.0 \pm 0.1 \text{ mm}$).
182 Specimens of 304SS were prepared by applying 0.5 mL with a syringe in a silicone mold
183 between two clamping plates to form an adhesive block $25 \times 5 \times 4 \text{ mm}^3$. A series of eight
184 samples was prepared and tested for each configuration.

185 These tests were conducted at room temperature ($23 \pm 2^\circ\text{C}$) with a tensile machine (INSTRON
186 3369, USA) equipped with a 500 N full-scale load cell with a sensitivity of 0.5%. The
187 displacement rate was $0.500 \pm 0.003 \text{ mm/min}$ in the three-point configuration (Figure 2 [right]).
188 The distance between supports was 35 mm (the norm indicating a space of 33 mm). The ultimate
189 load, F_{\max} , was considered as the failure initiation measurement [38]. The bending stress was
190 calculated by dividing the load by the adhesive surface area.

191 c. *Aging with the Bac Ford test (ISO 2812-2:2007)*

192 The Bac Ford test is used to analyze the aging and corrosion of automotive paintwork. It
193 comprises a tank where samples are immersed in demineralized water at 40°C with an angle of
194 $15\text{--}20^\circ$ for several days [34]. Our specimens are produced as described above with the addition
195 of a $24 \mu\text{m}$ film of glue to the surface to match real conditions as closely as possible. The

196 immersion time was set at 3 days.

197 3. *Surface characterization*

198 Treated surfaces were characterized by microstructural and chemical analysis using different
199 surface analytical techniques.

200 a. *Surface energy*

201 Surface energy measurements were conducted using the drop shape analyzer (DSA25) from
202 Krüss (Germany) in drop mode. The apparatus was equipped with a camera to perform
203 automatic measurements.

204 Several solvents were chosen to use the Owens, Wendt, Rabel, and Kaelble (OWRK) [40]
205 calculation method (Equations 1–2 and Table 3).

$$206 \quad \sigma_{sl} = \sigma_s + \sigma_l - 2 \left(\sqrt{\sigma_s^d \times \sigma_l^d} + \sqrt{\sigma_s^p \times \sigma_l^p} \right) \quad (\text{Equation 1})$$

207

208 σ_{sl} : Interfacial tension between liquid and solid phases

209 σ_s : Interfacial tension of solid phase

210 σ_l : Interfacial tension of liquid phase

211 σ_s^d : Dispersive component of solid phase

212 σ_l^d : Dispersive component of liquid phase

213 σ_s^p : Polar component of solid phase

214 σ_l^p : Polar component of liquid phase

215 Θ : Contact angle at triple point

216

$$217 \quad \sigma_{sl} = \sigma_s - \sigma_l \times \cos\theta \quad (\text{Equation 2})$$

218 A σ_l versus $\frac{\sigma_l^p}{\sqrt{\sigma_l^d}}$ curve was plotted to obtain the surface energy of the test specimen using drop
219 angles derived from the solvents used. Surface energies were obtained with a determination
220 coefficient R^2 exceeding 0.9.

221

222 Ideally, an apolar solvent should also be used; however, measurements with heptane and
223 cyclohexane are difficult due to low wettability angles.

224 Eight angle measurements were taken for the same drop. The contact angle measurement was
225 conducted by considering both angles of the drop on the substrate surface. The time interval
226 between points was 1.5 s, and each solvent was tested with four drops.

227 Therefore, it was possible to view the drops and measurements taken directly on the associated
228 Advance software. Surface energy calculations of the samples were obtained by the software.

229 b. *Friction test*

230 An Anton Paar circular tribometer was used to conduct a tribological study of different grafts
231 on the steel surface. After theoretical calculations based on the Hertz contact theory, a 5 mm
232 diameter 100Cr6 ball was used as a friction pin with a normal load of 1 N. Thus, the theoretical
233 mean pressure under contact was $P_{\text{mean}} = 440$ MPa. Before testing, the ball was cleaned with
234 ethanol and dried. The test speed was set at $v = 1$ $\text{rd}\cdot\text{s}^{-1}$ (leading to linear velocities of 12 to
235 20 $\text{mm}\cdot\text{s}^{-1}$ according to the friction track radius); 30 cycles were performed, and each test was
236 conducted at least three times.

237 c. *Microstructure analysis*

238 Field emission scanning electron microscopy with energy dispersive X-ray spectroscopy

239 (FESEM/EDX) was used to study the morphological surface using a Tescan Mira3 (Czech
240 Republic) instrument. Roughness was measured using an Infinite Focus optical microscope
241 from Alicona Imaging GmbH (France). X-ray photoelectron spectroscopy (XPS) was used to
242 measure the elemental composition to determine the surface compositions of the three-point
243 bending samples after testing. Spectra were acquired using monochromatized Al K α radiation
244 (1486.6 eV), and analyses were conducted at a photoelectron angle of 45°. The X-ray radiation
245 source operated in a vacuum of 3×10^{-9} mbar. The binding energies of core levels were
246 calibrated as a function of the C1s binding energy set at 284.8 eV, a characteristic energy of
247 alkyl moieties. Deconvolutions were performed using mixed Gaussian–Lorentzian curves (80%
248 Gaussian character) with CasaXPS software.

249 d. *Polarization modulation infrared reflection adsorption spectroscopy (PM-*
250 *IRRAS)*

251 PM-IRRAS orientation measurements were used to probe the orientation of bonds associated
252 with IR excitation of specific molecular vibrational modes. A Bruker Vertex 70 (USA) IR
253 spectrometer was used. The samples were positioned to obtain the largest signal amplitude; 36
254 scans were performed for each sample, and the resolution was 4 cm $^{-1}$. The detector was
255 positioned at an angle of 75°, according to results by F. Roy [36]. After acquisition, the spectra
256 were processed with the OPUS software. C-H vibration bands of CH $_3$ (wave numbers: $\nu_s = 2875$
257 cm $^{-1}$, $\nu_a = 2964$ cm $^{-1}$) and CH $_2$ ($\nu_s = 2851$ cm $^{-1}$, $\nu_a = 2921$ cm $^{-1}$) were analyzed to determine how
258 the SAMs were organized on the substrate surface [36].

259 e. *Glass transition temperature determination*

260 Differential scanning calorimetry (DSC) experiments were performed in a Mettler (DSC 1,
261 Switzerland) apparatus to determine the glass transition temperature (T_g) of Araldite with
262 various surface modifications. Aluminum pans containing a few mg of polymer were heated

263 from -10°C to 180°C at a heating rate of $10^{\circ}\text{C}\cdot\text{min}^{-1}$ under a continuous flow of oxygen and
264 argon in the first step. (This cycle is not considered in the study because two effects remain
265 possible: the end of the glue cross-linking and the removal of water from the sample.) After a
266 temperature drop, a second pass from -10°C to 180°C with a heating rate of $20^{\circ}\text{C}/\text{min}$ was
267 performed to get a better visualization of the glass transition event. Only the last step is
268 presented in this paper. The T_g was determined from the onset point (corresponding to the
269 beginning of the glass transition) for coatings from various treatments.

270

271 **III. Results**

272 Two sets of tests were conducted. The first focused on the impact of SAMs on 304SS
273 specimens. The second compared the two treatment processes: the classical one with phosphate
274 coated steel and the alternative process with stainless steel modified with SAMs.

275 The 304SS surface modification with SAMs can be used as an early grip layer before classical
276 cathaphoretic painting. Several SAMs were tested, in which the terminal function, carbon chain
277 length, or both were modified. A glue with the same epoxy base as this paint was used to ensure
278 a simpler study system.

279 The adherence study was conducted using two adherence tests, the SLJ and three-point bending.
280 Measurements were characterized before the test by PM-IRRAS and surface energy. A study
281 of metal/polymer interactions was also conducted by DSC with the glass transitions to
282 understand the phenomena observed during the adherence tests.

283 **1. Adherence test**

284 a. *Other parameters affecting adherence: post-modification rinsing*

285 Rinsed samples have better resistance to failure (21.5 ± 1.8 MPa) than unrinsed samples ($4.8 \pm$
286 1.8 MPa). Rinsing samples after surface modification removes species from solution together
287 with physisorbed clusters that form a weak attachment to the substrate (Figure 3). This layer
288 leads to poor adherence, though it is beneficial for obtaining the tribological properties [32; 41].

289 b. *Impact of carbon chain length*

290 Three SAMs of 4, 12, and 16 carbons were examined. Treatments were tested with the SLJ and
291 the three-point bending test. Results are expressed as stress (MPa) to compare the adherence of
292 SAMs in two failure modes (modes II and I).

293 Figure 4 shows the three-point bending and SLJ results for these three SAMs. The same order
294 of magnitude was observed for the SAMs/epoxy system and the 304SS/epoxy reference. The
295 stress involved is approximately 15 times greater in mode II (SLJ) stress than in mode I
296 (three-point bending). In the latter case, we divided by the adhesive surface area: $S = 5 \times 25 =$
297 125 mm². In reality, the fracture is initiated on a much smaller surface (Figure 5). The
298 restitution of elastic energy during three-point bending is transferred to the interface and
299 participates in the propagation of the fracture. Therefore, crack propagation is virtually
300 independent of the adhesive surface [42].

301 These tests cannot be compared in terms of values obtained as stresses vary. The results
302 obtained for the different treatment conditions are compared in each case.

303 In the three-point bending test, adding SAMs significantly improves the bending
304 strength. Without SAMs, the maximum bending stress is approximately 0.06 MPa, whereas

305 after adding SAMs, the maximum bending stress is between 1.0 and 1.1 MPa. Furthermore, the
306 carbon chain length does not appear to impact the bending stress.

307 In SLJ, adding SAMs with apolar endings to the surface of 304SS decreases the shear
308 stress, except for C12P, which does not alter the shear stress limit.

309 In the SLJ test, observing the test pieces may indicate mixed adhesive and cohesive fracture
310 modes, contrary to three-point bending samples (Figure 6). In the three-point bending test, tear-
311 offs are completely adhesive between the SAMs and epoxy polymer. In our case, no fracture
312 initiation on the three-point bending specimens was observed. SAMs are transparent and too
313 thin to be observed under a microscope. To quickly and easily check the sample fracture
314 location, we have developed an original test measuring the friction coefficient. Indeed, friction
315 coefficients are very different for steel (304SS), a polymer (Araldite), and a SAM. Thus, the
316 type of fracture can be ascertained by determining the friction coefficients on the surfaces of
317 the test specimens:

318 ♦ Adhesive: both surfaces have different coefficients.

319 ♦ Cohesive: both surfaces have the same friction coefficient.

320 Friction coefficients were measured at the point of adhesive failure on the test specimens after
321 the adherence test using an Anton Paar circular tribometer [43]. These test results are shown in
322 Figure 7. For the 304SS (reference without SAMs), the friction coefficient is around 0.5 after
323 30 cycles. For all SAMs except C4P, we found a friction coefficient below 0.2 after 30 cycles,
324 which is typical of the friction coefficient of a polymer such as Araldite glue for these load
325 conditions (see Figure 8). For the C4P treatment, differences exist in the friction coefficient,
326 which is closer to stainless steel than for the other SAMs tested.

327 Measurements were performed on the epoxy adhesive deposited on a 304SS specimen to verify

328 the friction coefficient. Different thicknesses of epoxy adhesive were deposited to observe what
329 adhesive film remained on the three-point bending specimens. Figure 8 shows the friction
330 coefficients obtained for specimens with an epoxy adhesive on surface films with thicknesses
331 of 24, 60, and 100 μm . These measurements were performed at least three times each.

332 According to Figure 8, the friction coefficient of the epoxy adhesive is below that observed on
333 the three-point bending test specimens. Furthermore, we were surprised to observe a slight
334 decrease in the friction coefficient as the adhesive film thickness decreased. Therefore, the
335 friction coefficient cannot be correlated with the film thickness remaining on the surfaces of
336 the three-point bending test specimens.

337 Based on these results, the fracture appears to be adhesive to the interphase SAM/adhesive for
338 C4P. For all the other SAMs, the friction coefficients are between 0.08 and 0.18, indicating
339 either an adhesive failure between the SAM and the adhesive or a cohesive failure in the
340 adhesive. Therefore, an XPS analysis of the specimen interface was conducted to verify these
341 results by another method.

342 The surface was characterized before testing to understand the interface present at the time of
343 bonding. Figure 9 represents the surface energy of SAMs with a chain length of 4 to 16 carbons.
344 Surface energies were obtained using the OWRK method [40] with three solvents (water,
345 ethylene glycol, and glycerol). Alkaline degreasing followed by ultrasonic degreasing in
346 ethanol was conducted to preserve the surface oxides and hydroxides [44]. Surface oxides create
347 a strong bond by chemisorption when SAMs are grafted to the surface. Moreover, we observed
348 that C4P has a higher surface energy than C12P. When the carbon chain length is small, a slight
349 overlap exists in the plate surface. Therefore, the substrate is visible, accounting for the
350 relatively high uncertainties for C4P. Indeed, C4P has a poor distribution on the surface of the
351 specimens [36], confirming the friction coefficients (intermediate between stainless steel and

352 SAMs). Observation of total surface energy indicates that the higher the carbon number in the
353 alkyl chain, the lower the total surface energy. However, the dispersive component of surface
354 energy has the same tendency as the three-point bending adherence results. Therefore, it appears
355 that the adherence achieved by adding SAMs is related to the dispersive energy of the interface
356 under test.

357 In the remainder of this study, C12P was retained, as this molecule provides good adherence in
358 the three-point bending test without altering shear adherence. The impact of the terminal
359 function was then tested with four different terminations: two apolar (alkyl and alkene) and two
360 polar (carboxylic and phosphonic acid).

361 c. *Impact of terminal groups*

362 The effect of the terminal function was tested using a chain length of 11–12 carbons with polar
363 (carboxylic and phosphonic acid) and apolar (alkyl and alkene) functions. Figure 10 compares
364 the maximum stresses at the fracture point for shear and three-point bending where the terminal
365 function was modified.

366 In SLJ, the terminal function has no impact, except for C9-CH=CH₂, where a slight increase in
367 shear stress is observed. In the three-point bending test, an improvement in bending stress is
368 observed for polar endings such as carboxylic and phosphonic acid functions. The polar endings
369 may therefore create interactions with the adhesive. Moreover, these two chemical functions
370 can react with one another by forming dimers for carboxyl functions, while phosphonic acid
371 groups can form bridges between them.

372 A friction test was conducted under the same conditions as before to verify that fracture occurs
373 in the SAM (see Figure 11).

374 According to Figure 11, adding SAMs allows a decrease in the friction coefficient approaching

375 0.2. Based on the above observations, this friction coefficient is obtained from the presence of
376 an epoxy adhesive film remaining on the surface of the specimens after the three-point bending
377 test. Except for C4P (Figure 7), failure of the three-point bending test specimen dots appears
378 cohesive in the adhesive.

379 XPS analysis of the chemical compositions of sample surfaces after three-point bending was
380 conducted to validate these hypotheses (Table 4).

381 The chemical composition presented in Table 4 shows an absence of phosphorus for C10COOH
382 and C12(2P) specimens. Furthermore, these specimens contain the same chemical species as
383 the epoxy adhesive, with approximately the same proportions of each element. The iron present
384 in the substrate is detected in very small quantities. This information indicates that, on the three-
385 point bending test specimens, failure is therefore cohesive in the epoxy adhesive. For C4P, a
386 low proportion of phosphorus exists, as well as the same chemical elements as the epoxy
387 adhesive, with an iron content higher than in C10COOH and C12(2P). This confirms that C4P
388 has an adhesive failure at the interphase of the SAMs and the adhesive, as elements of both the
389 adhesive and the SAMs are present in the failure zone. Evidence also exists that C4P is not
390 evenly distributed over the substrate surface due to the relatively high iron content.

391 These observations show that specimens with a friction coefficient of approximately 0.2 exhibit
392 cohesive failure in the adhesive in the three-point bending tests. For C4P, the friction coefficient
393 is between 0.2 (values for other SAMs) and 0.4 (values for the 304SS reference). This is
394 consistent with the chemical composition of the tested interface, indicating that the fracture is
395 adhesive in the SAM/adhesive interphase.

396 A surface energy study was then conducted on these two SAMs, as illustrated in Figure 12. This
397 showed a decrease in the total surface energy when treated with SAMs, compared to reference
398 304SS (without surface treatment on the specimen). Moreover, the decrease in the total surface

399 energy and polar component was lower when a polar carboxylic function was added. This
400 indicates that the terminal function is perpendicular to the surface.

401 Figures 10 and 12 demonstrate the impact of surface modification by SAMs. Therefore, the
402 latter improves adherence, especially with a chain length of 11 carbons with a carboxyl polar
403 terminal group, providing an adherence primer.

404 For Figures 4 and 10, we demonstrated that the termination of SAMs is more important than
405 the carbon chain length in obtaining a high maximum stress. Nothdurft showed that for two
406 polar carboxylic- terminated molecules, the best peel adherence results on copper were obtained
407 for C15COOH (16-phosphonohexadecanoic acid) compared to C5COOH (6-
408 phosphonohexanoic acid) [35]. Therefore, the question arose regarding whether a longer carbon
409 chain length in the presence of a carboxyl termination could improve the adherence of our
410 system.

411 Figure 13 compares bending stresses for C12P and C16P with those for C10COOH and
412 C14COOH, respectively. The results are compared to the reference without surface
413 modification with the 304SS.

414 As shown above, the carbon chain length with an apolar alkyl termination does not impact
415 three-point bending adherence. According to Figure 13, for a longer carbon chain with a polar
416 (carboxyl) termination, a decrease in bending stress is observed (for C14COOH compared to
417 C10COOH). Therefore, the carbon chain length plays a major role in polar terminations. A
418 decrease in adherence for C14COOH may originate from good SAM organization of long
419 carbon chains and the creation of hydrogen bonds between them, forming dimers [35].

420 d. *Comparison with reference coating: Phosphating process*

421 This study aims to replace the phosphate coating. The results were previously compared to the

422 reference system (Figure 14). On the left, the reference system comprises a zinc-phosphate
423 coating on low alloy steel. On the right, the replacement system comprises 304SS to improve
424 the anti-corrosion properties where SAMs are grafted on its surface.

425 A calculation was conducted to eliminate the substrates to compare these two systems and the
426 adherence results obtained in three-point bending tests. This calculation was performed to
427 obtain the adherence energy to compare both systems.

428 Figure 15 shows a standard three-point bending curve. The diagrams of the bonded assemblies
429 show each test stage up to the initiation of specimen failure. Force “Fa” represents the force
430 required to break the bonded assembly, while force “Fs” corresponds to the force required to
431 initiate the bending of the substrate only. To break the bonding joint, the deflection distance d
432 is required (measured by tensile machine). The following calculation obtains the energy
433 required to break the bonded assembly by separation from the substrate.

434 According to the publication by Alain Roche [45], the adherence energy is deduced from
435 Equation 3, which includes all the energies of specimen components. All these energies are
436 calculated for the same deflection, $d = d_{\text{failure}}$, for each tested specimen.

437
$$E_{\text{adherence}} = E_{\text{tot}} - E_{\text{substrate}} \quad (\text{Equation 1})$$

438

439 E_{tot} : total energy of the specimen

440 E_{substrat} : elastic deformation energy of the substrate

441

442 This calculation is used to formulate Equations 4 and 5, determining the adherence energy (E_a)
443 according to the treatment used by freeing the substrate.

444
$$E_{\text{adherence}} = \frac{(F_a \times d)}{2} - \frac{(F_s \times d)}{2} \quad (\text{Equation 2})$$

445
$$E_{adherence} = \frac{(F_a - F_s)d}{2} \quad (\text{Equation 5})$$

446 The results of the different tests were processed using equation 5 (figure 16). The results show
447 an improvement in adherence between modified 304SS and phosphating. The Adherence
448 energy increases when SAMs are grafted onto the surface. For an apolar alkyl-type termination,
449 the adherence energy increases with the carbon chain length.

450 For C12P and C9-CH=CH₂, the adherence energies are essentially the same. This result is
451 relatively consistent as the carbon chain length is similar, and the terminal function is apolar in
452 both cases. However, the standard deviation obtained is smaller. This may be due to the
453 presence of the double bond, which gives greater stability to the bonded assembly through
454 stabilizing π - π interactions, a privileged conformation, or both. Indeed, the rigidity of the
455 termination, which prevents its rotation in the assembly, leads to greater entanglement of the
456 molecules with one another and the adhesive.

457 In C10COOH, adding a carboxyl polar group allows a significant increase in adherence energy
458 compared to C12P (alkyl terminal function). This increase is probably because the carboxyl
459 termination reacts with the adhesive and forms dimers that stiffen the bonded assembly. This
460 observation applies to C12(2P), which also has a polar termination yielding a higher bond
461 energy than C12P. In this molecule, the polar phosphonic termination can react with the
462 adhesive but also form bridges on the substrate surface or create bonds between them. These
463 possibilities lead to rigidity of the bonded assembly with an inter-entanglement of molecules
464 longer than C12P.

465 An aging study of the three-point bending test specimens was conducted using the Bac
466 Ford test to identify the cumulative effect of SAMs in relation to the current phosphating
467 system.

468 e. *Aging of samples using the Bac Ford test*

469 A Bac Ford wet aging test was conducted for 3 days to place the specimens in more aggressive
470 conditions to reduce the adherence energies. Figure 17 shows the impact of 3-day aging in the
471 Bac Ford test in terms of adherence energy to compare these results with phosphating (reference
472 system). The results show that the coating from phosphating treatment is only slightly affected
473 by this wet aging, whereas, except for the C9-CH=CH₂ molecule, all other systems are more
474 heavily impacted.

475 C4P shows a slight decrease in adherence energy after aging for 3 days. We observed that the
476 longer the carbon chain length, the greater the impact of aging on the bonded assembly,
477 resulting in a sharp decrease in the system adherence energy. Evidently, the performance of
478 SAMs comprising molecules with a long carbon chain is significantly impacted by wet aging.

479 The coating containing the C10COOH molecules is seriously damaged by this aging, which
480 may be due to an acid-base reaction (by dissociation) occurring at the carboxylic acid
481 termination [$pK_{a1}(\text{COOH}) = 4.5\text{--}5$]. The results for C12(2P) are identical, as a significant
482 decrease in adherence energy is observed. This phenomenon must be due, first, to an acid-base
483 reaction of the terminal function of phosphonic acid [$Pka_1(\text{phosphonic}) = 2\text{--}3$] and, second, to
484 bond formation between terminations resulting in greater chain spacing, allowing incorporation
485 of water molecules into the thin film.

486 Contrary to these two coatings, the one comprising the C9-CH=CH₂ termination did not react
487 to this aging. The entanglement of these molecules, described above, and the apolar terminal
488 function make the coating visibly less accessible to water. A characterization study of interfaces
489 and grafting was conducted to verify the various hypotheses presented in this paper.

490 2. *Surface and interface characterization*

491 a. *SAM organization*

492 The various surface SAMs were observed by PM-IRRAS. CH₃ and CH₂ vibration bands were
493 analyzed to understand the organization of SAMs on the substrate surface. Indeed, CH₃ and
494 CH₂ vibrations of SAMs are characteristic when well-organized.

495 Symmetrical (s) and asymmetrical (a) vibration frequencies of the methylene group (CH₂)

496 systematically tend towards $\nu_s(\text{CH}_2) = 2850 \text{ cm}^{-1}$ and $\nu_a(\text{CH}_2) = 2920 \text{ cm}^{-1}$, according to

497 Spori *et al.* [41]. Frequency variation is known to be sensitive to the conformational order of

498 alkyl chains, shifting to higher frequencies with a conformational disorder. Symmetrical and

499 asymmetrical vibration frequencies of the methyl group (CH₃) tend towards

500 $\nu_s(\text{CH}_3) = 2870 \text{ cm}^{-1}$ and $\nu_a(\text{CH}_3) = 2960 \text{ cm}^{-1}$, while their positions remain almost invariable

501 depending on the chain conformation according to Spori *et al.* [46].

502 The observed values of CH₃ vibration bands are almost constant, of the order of 2960 cm^{-1} ,

503 with minimal variation depending on the SAMs tested. The length of the carbon chain

504 influenced the locations of the CH₂ vibration bands, especially the symmetrical one. Indeed,

505 the vibration frequency appears at 2859 cm^{-1} for short chains such as C4P, a high value being

506 characteristic of a disordered alkyl chain [46]. For chain lengths exceeding 12 atoms

507 (C14COOH, C16P, and C20P), vibration bands appear at 2850 cm^{-1} , indicating that these

508 molecules adopt a crystalline, well-organized structure. For intermediate chains with a length

509 of 11–12 carbons, the sym-band is located at a value between 2850 and 2860 cm^{-1} , indicating a

510 semi-crystalline structure [C10COOH: $\nu_s(\text{CH}_2) = 2854 \text{ cm}^{-1}$; C12P: $\nu_s(\text{CH}_2) = 2860 \text{ cm}^{-1}$].

511 Several research teams observed these phenomena and concluded that short carbon chains of

512 SAMs are disordered, whereas long carbon chains ($C > 11-12$) produce well-organized

513 structures on the surface of the substrate [36] [46-55]. For intermediate chain lengths, a mixed

514 organization is observed with a semi-crystalline system.

515 b. *Study of metal/polymer interaction: glass transitions*

516 DSC was conducted using a Mettler instrument (DSC 1) to determine the T_g of Araldite in
517 contact with the various SAMs. When in contact with the SAMs, the epoxy network changed,
518 leading to a difference in T_g [56-58].

519 The difference in T_g may be due to the following:

- 520 • Stiffness of SAMs,
- 521 • Molecular mass of SAMs,
- 522 • Decrease in free volume between SAMs and epoxy,
- 523 • Decreased mobility of SAMs with increased reticulation,

524 or a combination of the above conditions [59].

525 The adhesive undergoes the same curing cycle as in the adherence tests. Therefore, it must have
526 the same T_g regardless of the surface treatment.

527 Measurements of the T_g of the glue/substrate interphase with varying glue thicknesses were
528 compared to values obtained by the glue in its volume (Figure 18). These measurements
529 indicated that the T_g of the interphase is higher at lower glue thicknesses, leading to stable
530 mechanical properties in a larger temperature range. In this study, an optimum value was
531 obtained for a 24 μm glue thickness. Subsequently, the remainder of this study was conducted
532 with 24 μm films for comparison with samples used for adherence to simulate a glue joint
533 “towards the glue/SAM interface” (Figure 19).

534 An optimum T_g of $96 \pm 1^\circ\text{C}$ was obtained for C12(2P). C12(2P) can form bridges on the
535 substrate surface through phosphonic acid functions. Building network rigidity leads to reduced

536 mobility of SAMs and accounts for the greater T_g .

537 PM-IRRAS measurements showed a mixed organization for a chain length of 11–12 carbons,
538 which favors an increase in the layer density of SAMs, as for C12P. SAMs have a similar T_g to
539 304SS.

540

541

542 **IV. Discussion and visualization of SAM organization**

543 ***1. Results overview***

544 The analyses and tests showed an improvement in adherence after adding SAMs, depending
545 on SAMs organization. Let us know that the SAMs organization is directly linked to their
546 composition (carbon chain length and terminal function). Table 5 provides an overview of
547 these results.

548 ***2. Visualization of SAM organization***

549 The various adherence tests and the characterization study of surfaces in terms of surface
550 energy, PM-IRRAS, DSC, and XPS allow us to propose an organization model of the different
551 SAMs tested (Table 6).

552 Short-chain molecules (C4P) do not completely cover the substrate surface. Previous studies
553 show that C4P is not correctly organized on the surface [36]. The molecules become entangled
554 and agglomerate.

555 Long-chain SAMs (C16P) allow Van der Waals interactions, permitting orientated organization
556 of molecules in relation to one another. In terms of adherence, this good organization of apolar

557 terminations does not ensure good adherence with the epoxy, which was also observed with
558 carboxylic terminations (C14COOH).

559 For SAMs of average carbon chain length [C12P, C9-CH=CH₂, C10COOH, and C12(2P)],
560 PM-IRRAS and XPS are inadequate with chain entanglement, as well as with the presence of
561 organized molecules. This combination of both types of configuration results in superior
562 adherence compared to other chain lengths.

563 Such a combination of organizations in the presence of a polar termination (carboxylic and
564 phosphonic acid) results in an adherence primer capable of surpassing phosphatization
565 regarding three-point bending stresses.

566 This modeling confirms several studies with a short chain length. SAMs do not organize
567 themselves or completely cover the substrate surface [46; 60]. With a chain length exceeding
568 14 carbons, SAMs are organized automatically through London interactions. An intermediate
569 chain length allows a good overlap due to mixed organization [36]. Moreover, adding a polar
570 termination allows the creation of new interactions between molecules of the Keesom and
571 Debye type, which will generate good cohesion of the bonded assembly.

572 **V. Conclusions**

573 In this study, alkylphosphonic acids were investigated to replace steel-phosphating treatments.
574 Before the modification treatment, 304SS substrates were immersed in an alkaline degreasing
575 bath. After modification with alkylphosphonic acids, we confirmed that it is essential to conduct
576 optimized rinsing to remove physisorbed clusters from the surface to obtain a good-quality thin
577 film with better adherence.

578 This research studied practical adhesion with two adherence tests: the SLJ and three-point
579 bending tests. To simulate the industrial conditions of cathoretic painting, we used an epoxy-

580 based glue, Araldite 103-1, with a hardener, HY 991, which also has an epoxy function.
581 Phosphating treatment is replaced with SAMs where the carbon chain length and the terminal
582 function have been modified. According to the three-point bending tests, confirmed by friction
583 coefficient measurements at the break site, fractures are cohesive in the adhesive, except for
584 C4P, where the fracture is adhesive in the SAM/adhesive interphase. The shear test results show
585 that SAMs comprising molecules with short or long carbon chain lengths lead to decreased
586 adherence compared to 304SS. The results for a median chain length (C12P) are comparable to
587 the substrate. Terminations do not appear to impact the maximum shear stress, whereas a slight
588 improvement could be observed with C9-CH=CH₂.

589 In three-point bending, adding SAMs improves adherence. A carbon chain with an apolar
590 termination minimally impacts the maximum shear stress. A polar termination with a length of
591 11–12 carbons has been shown to improve adherence. In both tests, grafting with
592 alkylphosphonic acids appears to be optimized with a chain length of 11–12 carbons.

593 The surface energy is consistent with the adherence results and allows modeling of the
594 organization of the different SAMs. A chain length of 11–12 carbons gives a semi-crystalline
595 organization of SAMs.

596 Adherence energy results enabled the comparison of the two systems studied: phosphate coating
597 on steel and SAMs grafted on stainless steel. It appears that treatment with SAMs significantly
598 improves system adherence. Nevertheless, the replacement system is more sensitive to wet
599 aging than the phosphate coating, except for C9-CH=CH₂, which shows higher adherence after
600 aging.

601 In three-point bending, a terminal polar function of a carboxylic or phosphonic acid type allows
602 a good adherence primer to be obtained.

603 Finally, the optimal condition for better adhesion is a mixture of ordered and entangled SAMs.
604 Reducing the grafting time to 30 seconds could allow this configuration to be obtained, making
605 the treatment compatible with industrial conditions.

606

607 Acknowledgment

608 The authors wish to thank Aurélien Buteri from APERAM Inc. for the supply of 304SS; Nicolas
609 Rouge for SEM images; Vincent Tissot for machining of installations for bonded assembly
610 samples, as well as for shear bites; and Olivier Heintz for XPS analysis.

611

612

613 Declaration of interest statement

614 The authors declare that they have no known competing financial interests or personal
615 relationships that could have appeared to influence the work reported in this paper.

616

617

618 References

619

620 [1] Thomas Watts Coslett. Treatment of iron or steel for preventing oxidation or rusting.
621 November 12 1907. US Patent 870,937.

622 [2] TSN Sankara Narayanan. Surface pretreatment by phosphate conversion coatings-a
623 review. *Reviews in Advanced Materials Science*, 9:130–177, 2005.

624 [3] Feng Fang, Jing-hua Jiang, Shu-Yong Tan, Ai-bin Ma, and Jian-qing Jiang.
625 Characteristics of a fast low-temperature zinc phosphating coating accelerated by an
626 eco-friendly hydroxylamine sulfate. *Surface and Coatings Technology*, 204(15):2381–
627 2385, 2010.

628 [4] I Milošev and GS Frankel. Conversion coatings based on zirconium and/or titanium.
629 *Journal of The Electrochemical Society*, 165(3):C127–C144, 2018.

630 [5] L Fedrizzi, FJ Rodriguez, S Rossi, F Deflorian, and R Di Maggio. The use of
631 electrochemical techniques to study the corrosion behaviour of organic coatings on steel

- 632 pretreated with sol-gel zirconia films. *Electrochimica Acta*, 46(24-25):3715–3724,
633 2001.
- 634 [6] Masahiko Matsukawa, Kazuhiro Makino, and Toshiaki Shimakura. Chemical
635 conversion coating agent and surface-treated metal, December 23 2004. US Patent
636 2004,018,7967.
- 637 [7] Donald R Vonk, Edis Kapic, Bruce Goodreau, and Alvaro Bobadilla. Metal
638 pretreatment composition containing zirconium, copper, zinc, and nitrate and related
639 coatings on metal substrates, June 25 2012. US Patent 2012,030,1739.
- 640 [8] Donald R Vonk, Edis Kapic, and Michael L Sienkowski. Metal pretreatment
641 composition containing zirconium, copper, and metal chelating agents and related
642 coatings on metal substrates, March 12 2013. US Patent 2013,026,6819.
- 643 [9] HR Asemani, P Ahmadi, AA Sarabi, and H Eivaz Mohammadloo. Effect of zirconium
644 conversion coating: Adhesion and anti-corrosion properties of epoxy organic coating
645 containing zinc aluminum polyphosphate (zapp) pigment on carbon mild steel. *Progress
646 in Organic Coatings*, 94:18–27, 2016.
- 647 [10] Hossein Eivaz Mohammadloo, Ali Asghar Sarabi, Ali Asghar Sabbagh Alvani, Hassan
648 Sameie, and Reza Salimi. Nano-ceramic hexafluorozirconic acid based conversion thin
649 film: Surface characterization and electrochemical study. *Surface and Coatings
650 Technology*, 206(19-20):4132–4139, 2012.
- 651 [11] Patrick Droniou, William E Fristad, and Jeng-Li Liang. Nanoceramic-based conversion
652 coating: Ecological and economic benefits position process as a viable alternative to
653 phosphating systems. *Metal finishing*, 103(12):41–43, 2005.
- 654 [12] VONK Donald, Edis Kapic, Bruce Goodreau, and Alvaro Bobadilla. Metal pretreatment
655 composition containing zirconium, copper, zinc and nitrate and related coatings on
656 metal substrates, August 23 2018. US Patent App. 15/961,262.
- 657 [13] Nguyen Van Chi, Pham Trung San, To Thi Xuan Hang, Truong Anh Khoa, Nguyen
658 Hoang, Nguyen Thu Hien, et al. Corrosion protection of carbon steel using zirconium
659 oxide/silane pretreatment and powder coating. *Vietnam Journal of Science and
660 Technology*, 57(1):38, 2019.
- 661 [14] WJ Van Ooij, Danqing Zhu, M Stacy, A Seth, T Mugada, J Gandhi, and P Puomi.
662 Corrosion protection properties of organofunctional silanes An overview. *Tsinghua
663 Science and technology*, 10(6):639–664, 2005.
- 664 [15] B Ramezanzadeh, E Raeisi, and M Mahdavian. Studying various mixtures of 3-
665 aminopropyltriethoxysilane (aps) and tetraethylorthosilicate (teos) silanes on the

- 666 corrosion resistance of mild steel and adhesion properties of epoxy coating.
667 *International Journal of Adhesion and Adhesives*, 63:166–176, 2015.
- 668 [16] Cecilia Deyá. Silane as adhesion promoter in damaged areas. *Progress in Organic*
669 *Coatings*, 90:28–33, 2016.
- 670 [17] C Motte, M Poelman, A Roobroeck, M Fedel, F Deflorian, and M-G Olivier.
671 Improvement of corrosion protection offered to galvanized steel by incorporation of
672 lanthanide modified nanoclays in silane layer. *Progress in Organic Coatings*,
673 74(2):326–333, 2012.
- 674 [18] Vera Rosa Capelossi and Idalina Vieira Aoki. Influence of sonication on anticorrosion
675 properties of a sulfursilane film dopped with ce (iv) on galvanized steel. *Progress in*
676 *Organic Coatings*, 76(5):812–820, 2013.
- 677 [19] Juliana S Francisco, Vera Rosa Capelossi, and Idalina Vieira Aoki. Evaluation of a
678 sulfursilane anticorrosive pretreatment on galvanized steel compared to phosphate
679 under a waterborne epoxy coating. *Electrochimica Acta*, 124:128–136, 2014.
- 680 [20] MGS Ferreira, RG Duarte, MF Montemor, and AMP Simoes. Silanes and rare earth
681 salts as chromate replacers for pre-treatments on galvanized steel. *Electrochimica acta*,
682 49(17-18):2927–2935, 2004.
- 683 [21] Abraham Ulman. Formation and structure of self-assembled monolayers. *Chemical*
684 *reviews*, 96(4):1533–1554, 1996.
- 685 [22] Frank Schreiber. Structure and growth of self-assembling monolayers. *Progress in*
686 *surface science*, 65(5-8):151–257, 2000.
- 687 [23] Sidharam P Pujari, Luc Scheres, Antonius TM Marcelis, and Han Zuilhof. Covalent
688 surface modification of oxide surfaces. *Angewandte Chemie International Edition*,
689 53(25):6322–6356, 2014.
- 690 [24] CR Kaufmann, G Mani, D Marton, DM Johnson, and CM Agrawal. Long-term stability
691 of self-assembled monolayers on 316l stainless steel. *Biomedical Materials*,
692 5(2):025008, 2010.
- 693 [25] John G Van Alsten. Self-assembled monolayers on engineering metals: structure,
694 derivatization, and utility. *Langmuir*, 15(22):7605–7614, 1999.
- 695 [26] Clémence Queffélec, Marc Petit, Pascal Janvier, D Andrew Knight, and Bruno Bujoli.
696 Surface modification using phosphonic acids and esters. *Chemical reviews*,
697 112(7):3777–3807, 2012.

- 698 [27] Seid Yimer Abate, Ding-Chi Huang, Yu-Tai Tao, Surface modification of TiO₂ layer
699 with phosphonic acid monolayer in perovskite solar cells: Effect of chain length and
700 terminal functional group, *Organic Electronics*, 78:105583, 2019
- 701 [28] Gaëlle Anne Léonie Andreatta, Nicolas Blondiaux, Antonin Faes, Spray coating vs.
702 immersion for self-assembly of gemini perfluorinated phosphonic acids on indium tin
703 oxide, *Thin Solid Films*, 732: 138783, 2021
- 704 [29] Dajana Mikić, Helena Otmačić Ćurković, Saman Hosseinpour, Bronze corrosion
705 protection by long-chain phosphonic acids, *Corrosion Science*, 205: 110445, 2022
- 706 [30] Mohamed Moustapha Moine, Xavier Roizard, Jean-Marie Melot, Luc Carpentier,
707 Pierre-Henri Cornuault, Fabrice Lallemand, Jean-Marie Rauch, Olivier Heintz, and
708 Séverine Lallemand. Grafting and characterization of dodecylphosphonic acid on
709 copper: Macro-tribological behavior and surface properties. *Surface and Coatings*
710 *technology*, 232:567–574, 2013.
- 711 [31] Durainatarajan, Periyasamy; Prabakaran, Mallaiah; Ramesh, Subbaratnam, Self-
712 assembled monolayers of novel imidazole derivative on copper surface for anticorrosion
713 protection in neutral medium, *Journal of Adhesion Science & Technology*, 35(23): 2580-
714 2601, 2021
- 715 [32] Hrimla, Meryem; Bahsis, Lahoucine; Boutouil, Aziz; Laamari, My Rachid; Julve,
716 Miguel, A combined computational and experimental study on the mild steel corrosion
717 inhibition in hydrochloric acid by new multifunctional phosphonic acid containing
718 1,2,3-triazoles, *Journal of Adhesion Science & Technology*, 34(16): 1741-1773, 2020
- 719 [33] Fabrice Lallemand, Xavier Roizard, Jean-marie Melot, Aurélien Buteri, Mélanie
720 Borgeot, and Romain Evrard. Surface treatment of metal substrates, February 5 2019.
721 US Patent 10,196,744.
- 722 [34] Evelin Jaehne, Sonia Oberoi, and Hans-Juergen P Adler. Ultra thin layers as new
723 concepts for corrosion inhibition and adhesion promotion. *Progress in Organic*
724 *Coatings*, 61(2-4):211–223, 2008.
- 725 [35] Philipp Nothdurft, Sonja Feldbacher, Georg Jakopic, Inge Mühlbacher, Sandra Pötz,
726 and Wolfgang Kern. Surface characterization of copper substrates modified with
727 carboxyl terminated phosphonic acids. *International Journal of Adhesion and*
728 *Adhesives*, 84:143–152, 2018.

- 729 [36] Florian Roy, Abdeslam Et Taouil, Fabrice Lallemand, Jean-Marie Melot, Xavier
730 Roizard, Olivier Heintz, Virginie Moutarlier, and Jean-Yves Hihn. Influence of
731 modification time and high frequency ultrasound irradiation on self-assembling of
732 alkylphosphonic acids on stainless steel: Electrochemical and spectroscopic studies.
733 *Ultrasonics sonochemistry*, 28:269–275, 2016.
- 734 [37] Daniel Garcia-Raya, Rafael Madueo, José Manuel Sevilla, Manuel Blizquez, and
735 Teresa Pineda. Electrochemical characterization of a 1,8-octanedithiol self-assembled
736 monolayer (odt-sam) on a au(111) single crystal electrode. *Electrochimica Acta*,
737 53(27):8026 – 8033, 2008.
- 738 [38] Sébastien Genty, Jean-Baptiste Sauvage, Philippe Tingaut, and Maëlen Aufray.
739 Experimental and statistical study of three adherence tests for an epoxy-
740 amine/aluminum alloy system: Pull-off, single lap joint and three-point bending tests.
741 *International Journal of Adhesion and Adhesives*, 79:50–58, 2017.
- 742 [39] Evelyne DARQUE-CERETTI and Bernard MONASSE. Mise en peinture
743 des plastiques. *Techniques de l'ingénieur Finitions des plastiques, conceptions des*
744 *pièces et recyclage*, base documentaire: TIB475DUO.(ref. article: am3785), 2010. fre.
- 745 [40] Daniel K Owens and RC Wendt. Estimation of the surface free energy of polymers.
746 *Journal of applied polymer science*, 13(8):1741–1747, 1969.
- 747 [41] Pierre-Henri Cornuault, Jean-Marie Melot, Xavier Roizard, and Fabrice Lallemand. Dry
748 lubrication of ferritic stainless steel functionalised with crystalline aggregates of
749 hexadecylphosphonic acid. *Tribology International*, 145:106139, 2020.
- 750 [42] Jean-Baptiste Sauvage. *Caractérisation et modélisation de l'adhérence dans les*
751 *assemblages collés*. PhD thesis, Mulhouse, 2016.
- 752 [43] Xavier Roizard, Jannica Heinrichs, Aurélien Butéri, Staffan Jacobson, Mélanie Borgeot,
753 Luc Carpentier, Jean-Marie Melot, and Fabrice Lallemand. Friction behavior of ferritic
754 stainless steel in a strongly diluted alcohol solution of alkylphosphonic acid. *Tribology*
755 *International*, 118:465–473, 2018.
- 756 [44] M Mantel and JP Wightman. Influence of the surface chemistry on the wettability of
757 stainless steel. *Surface and Interface analysis*, 21(9):595–605, 1994.
- 758 [45] A Roche, F Gaillard, M Romand, and M Von Fahnestock. Metal-adhesive bonded
759 systems: Adhesion measurement using a three point flexure test. *Journal of Adhesion*
760 *Science and Technology*, 1(1):145–157, 1987.

- 761 [46] Doris M Spori, Nagaiyanallur V Venkataraman, Samuele GP Tosatti, Firat Durmaz,
762 Nicholas D Spencer, and Stefan Zürcher. Influence of alkyl chain length on phosphate
763 self-assembled monolayers. *Langmuir*, 23(15):8053–8060, 2007.
- 764 [47] Peter Thissen, Markus Valtiner, and Guido Grundmeier. Stability of phosphonic acid
765 self-assembled monolayers on amorphous and single-crystalline aluminum oxide
766 surfaces in aqueous solution. *Langmuir*, 26(1):156–164, 2010.
- 767 [48] Nolan Tillman, Abraham Ulman, Jay S Schildkraut, and Thomas L Penner.
768 Incorporation of phenoxy groups in self-assembled monolayers of trichlorosilane
769 derivatives. Effects on film thickness, wettability, and molecular orientation. *Journal of*
770 *the American Chemical Society*, 110(18):6136–6144, 1988.
- 771 [49] Rosalynn Quinones and Ellen S Gawalt. Study of the formation of self-assembled
772 monolayers on nitinol. *Langmuir*, 23(20):10123–10130, 2007.
- 773 [50] Houston Byrd, John K Pike, and Daniel R Talham. Inorganic monolayers formed at an
774 organic template: a langmuir-blodgett route to monolayer and multilayer films of
775 zirconium octadecylphosphonate. *Chemistry of materials*, 5(5):709–715, 1993.
- 776 [51] Ralph G Nuzzo, Lawrence H Dubois, and David L Allara. Fundamental studies of
777 microscopic wetting on organic surfaces. 1. Formation and structural characterization
778 of a self-consistent series of polyfunctional organic monolayers. *Journal of the*
779 *American Chemical Society*, 112(2):558–569, 1990.
- 780 [52] Marc D Porter, Thomas B Bright, David L Allara, and Christopher ED Chidsey.
781 Spontaneously organized molecular assemblies. 4. Structural characterization of n-alkyl
782 thiol monolayers on gold by optical ellipsometry, infrared spectroscopy, and
783 electrochemistry. *Journal of the American Chemical Society*, 109(12):3559–3568,
784 1987.
- 785 [53] Michael Maxisch, Christoph Ebbert, Boray Torun, Nicole Fink, Teresa De Los Arcos,
786 J Lackmann, Hans Jürgen Maier, and Guido Grundmeier. Pm-irras studies of the
787 adsorption and stability of organophosphonate monolayers on passivated niti surfaces.
788 *Applied Surface Science*, 257(6), 2011.
- 789 [54] Ch Bram, Ch Jung, and M Stratmann. Self assembled molecular monolayers on
790 oxidized inhomogeneous aluminum surfaces. *Fresenius' journal of analytical*
791 *chemistry*, 358(1-2):108–111, 1997.
- 792 [55] Zineb Mekhalif, Gregory Fonder, Fabrice Laffineur, and Joseph Delhalle. Comparative
793 assessment of n-dodecanethiol and n-dodecaneselenol monolayers on electroplated
794 copper. *Journal of Electroanalytical Chemistry*, 621(2):245–253, 2008.

- 795 [56] Hamid Bourahla, Jeanine Lenoir, Maurice Romand, and Jean Chauchard. Influence de
796 l'épaisseur de l'adhésif et du vieillissement sur les propriétés mécaniques dynamiques
797 d'un assemblage: adhésif structural/acier inoxydable. *Die Angewandte*
798 *Makromolekulare Chemie: Applied Macromolecular Chemistry and Physics*,
799 178(1):47–62, 1990.
- 800 [57] AA Roche, J Bouchet, and S Bentadjine. Formation of epoxy-diamine/metal
801 interphases. *International Journal of Adhesion and Adhesives*, 22(6):431–441, 2002.
- 802 [58] J Bouchet and A.A. Roche. The formation of epoxy/metal interphases: mechanisms and
803 their role in practical adhesion. *The Journal of Adhesion*, 78(9):799–830, 2002.
- 804 [59] Ch Oudet. Polymers structure and properties introduction; polymeres structure et
805 proprietes introduction. 1993.
- 806 [60] Colin D Bain and George M Whitesides. Modeling organic surfaces with self-
807 assembled monolayers. *Angewandte Chemie*, 101(4):522–528, 1989.
- 808 [61] S Frey, A Shaporenko, M Zharnikov, P Harder, and DL Allara. Self-assembled
809 monolayers of nitrile-functionalized alkanethiols on gold and silver substrates. *The*
810 *Journal of Physical Chemistry B*, 107(31):7716–7725, 2003.

811

812 Table 1: Chemical composition and roughness parameters of samples

	Fe	Cr	Ni	Sa (arithmetic mean height)	Sq (root mean square height)	Ssk (Skewness)	Sku (Kurtosis)
304 SS plate	72.93 %	18.47 %	8.60 %	4.49 μm	5.89 μm	0.08	4.44
304 SS bare	72.80 %	18.54 %	8.66 %	5.91 μm	7.45 μm	0.08	3.12

813 Table 2: Different SAMs

Molecules names	
Butanephosphonic acid	C4P
Dodecanephosphonic acid	C12P
Hexadecanephosphonic acid	C16P
11-phosphonoundecanoic acid	C10COOH
Dodecane-1,12-diphosphonic acid	C12(2P)
10-undecanephosphonic acid	C9CH=CH2
15-phosphonopentadecanoic acid	C14COOH

814 Table 3: Solvents interfacial tensions

Solvents	Interfacial tension σ_1 (mJ/m ²)	Dispersive component σ_1^d (mJ/m ²)	Polar component σ_1^p (mJ/m ²)
water	72.8	21.8	51
ethylene glycol	48.3	29.3	19
glycerol	63.4	37	26.4

815

816

817

818

819 Table 4: Analysis of sample composition by XPS in atomic percent (measurement uncertainties
 820 of 0.1 %)

	C1s	N1s	O1s	Si2p	P2p	Fe2p
C10COOH	68.1	2.6	21.0	8.0	-	0.2
C12(2P)	68.9	2.6	19.7	8.5	-	0.2
C4P	43.7	3.2	40.4	7.2	0.8	4.7
Epoxy adhesive	71.2	2.5	18.2	8.1		

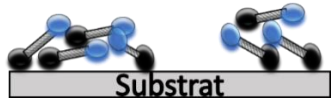
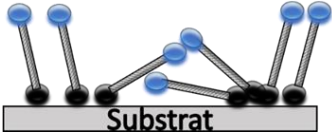
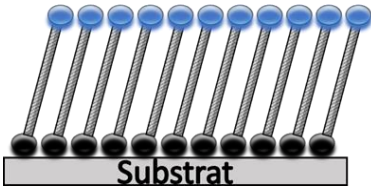
821

822 Table 5: Results overview

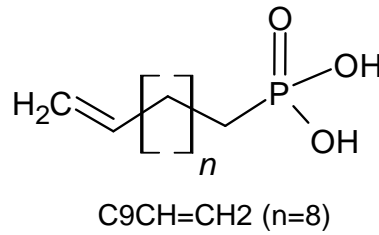
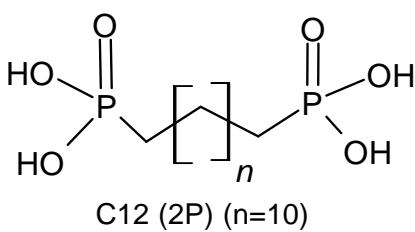
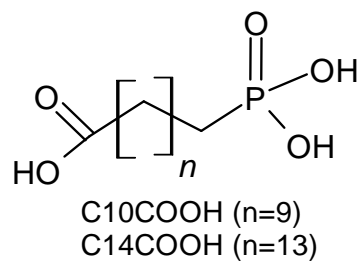
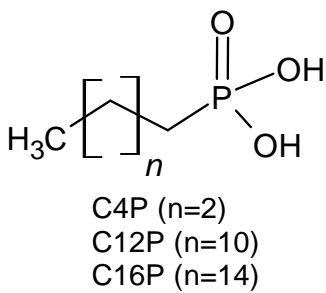
Samples	Tensile stress test (MPa)	Three-Point bending test (MPa)	Surface energy (mN/m)	Dispersive part (mN/m)	Polar part (mN/m)	Adherence energy (mJ)		Glass transition (°C)	ν_s (CH ₂) (cm ⁻¹)
						Without ageing	Ageing		
304SS (Reference)	20.3 ± 0.9	0.60 ± 0.07	50.67 ± 2.42	3.84 ± 0.56	46.82 ± 1.86	7.4 ± 2.9	0.6 ± 0.7	89 ± 1	/
Phosphatation	/	/	/	/	/	3.5 ± 0.9	2.4 ± 1.2		/
Reference values	/	/	/	/	/	/	/	/	2850
C4P	16.2 ± 1.4	1.03 ± 0.20	28.34 ± 30.35	10.19 ± 12.58	18.14 ± 2	21.4 ± 25.7	14.6 ± 4.2	88 ± 1	2859
C10COOH	20.7 ± 2.1	1.62 ± 0.15	33.8 ± 3.05	10.91 ± 1.3	22.89 ± 1.76	97.7 ± 30.7	2.7 ± 0.5	89 ± 1	2854
C12P	20.7 ± 1.0	0.93 ± 0.40	22.10 ± 4.34	9.94 ± 2.34	12.15 ± 2	29.8 ± 30.1	12.7 ± 6.9	92 ± 1	2860
C14COOH	/	0.21 ± 0.02	/	/	/	/	/	/	2849
C16P	13.7 ± 2.7	1.08 ± 0.10	21.05 ± 1.1	15.57 ± 0.74	5.47 ± 0.36	42.6 ± 7.8	0.3 ± 3.9	89 ± 1	2850
C9-CH=CH2	23.1 ± 2.6	1.02 ± 0.20	/	/	/	29.0 ± 17.1	34.6 ± 7.7	87 ± 1	/
C12(2P)	17.6 ± 0.9	1.48 ± 0.14	/	/	/	74.4 ± 21.9	2.6 ± 2.3	96 ± 1	/

823

824 Table 6: Modelling organisation of SAMs

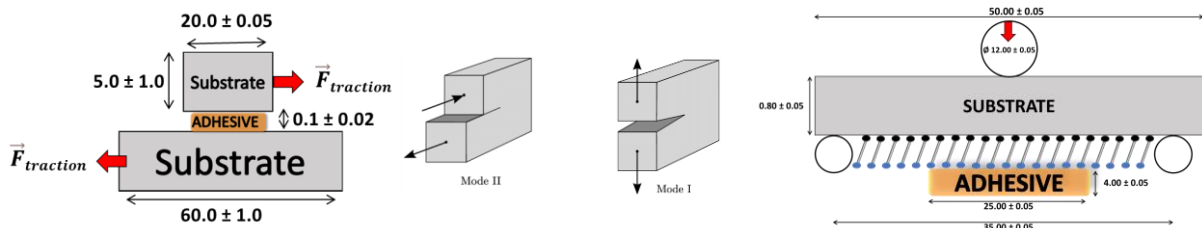
C4P	C12P / C10COOH / C12(2P) / C9-CH=CH2	C16P / C14COOH / C20P
		

825



826

827 Figure 1: Different alkylphosphonic acids

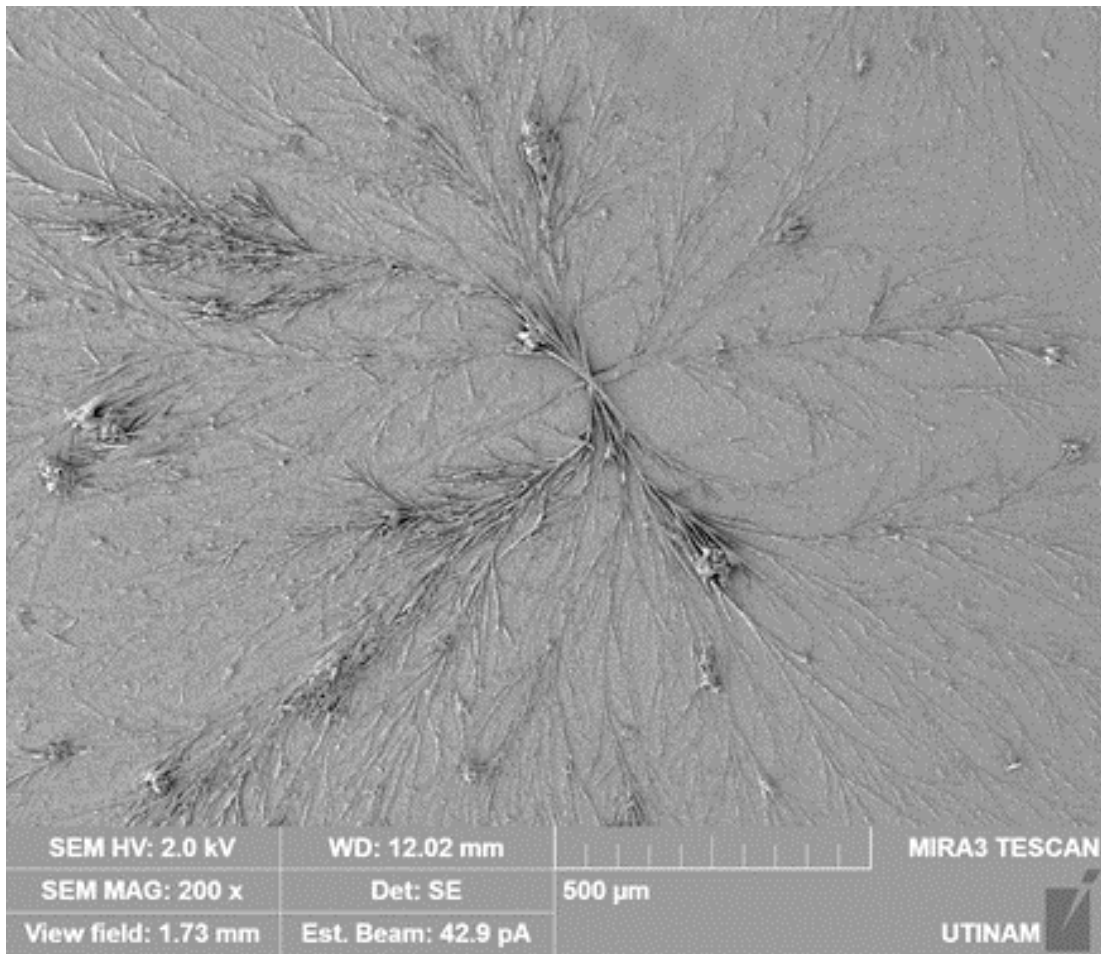


828

829 Figure 2: Single Lap Joint geometry, (not to scale, dimensions in mm) mode II sollicitation

830 (Left) and Three-point bending geometry (not to scale, dimensions in mm), mode I and II

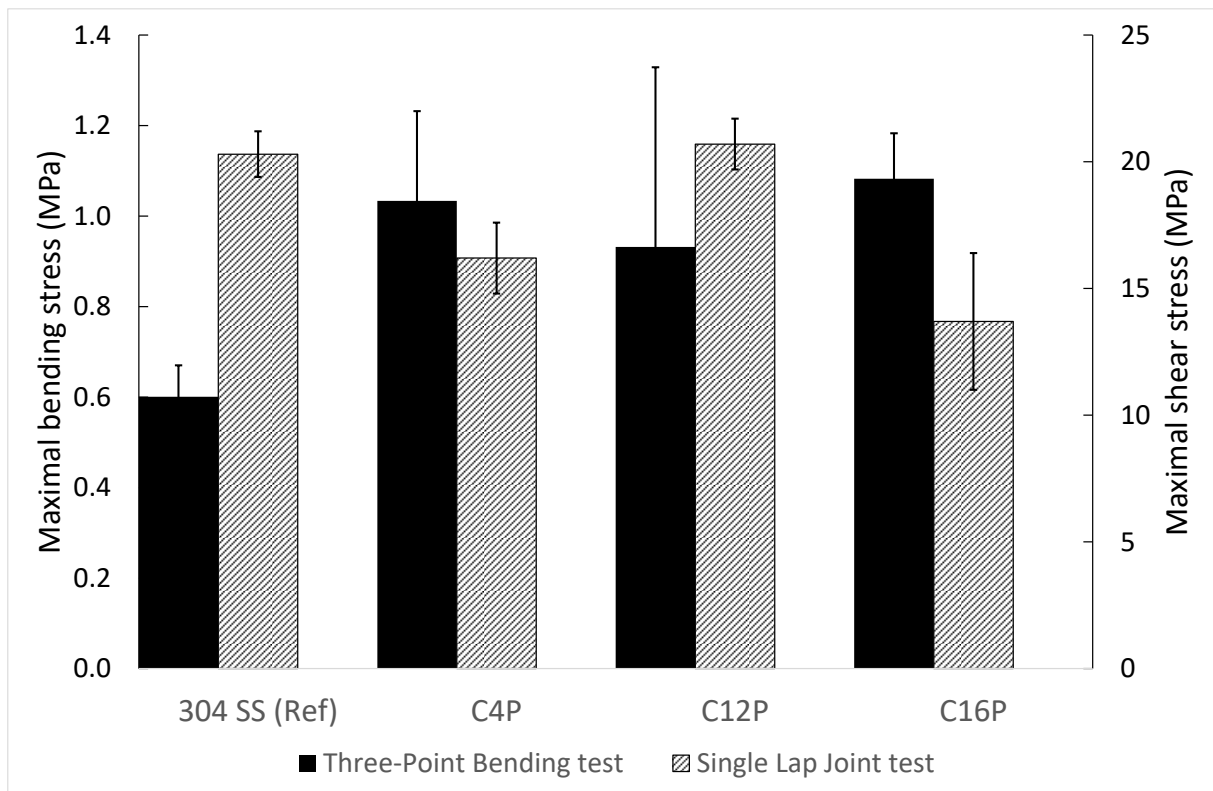
831 sollicitation (Right)



832

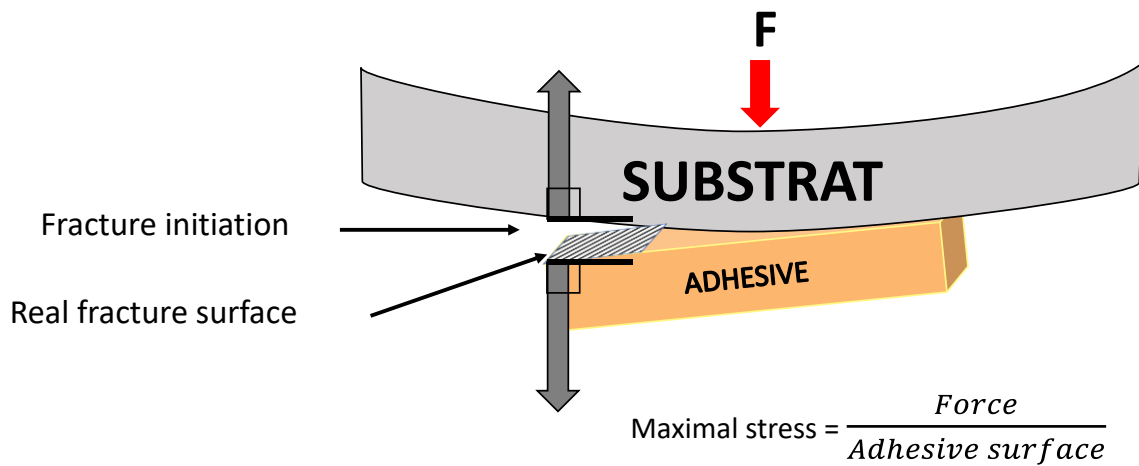
833 Figure 3: SEM picture of a physisorbed cluster on the surface sample without rinsing post

834 modification



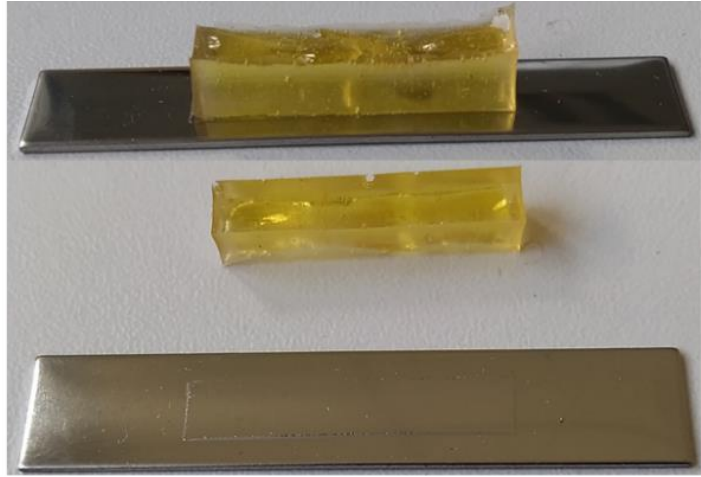
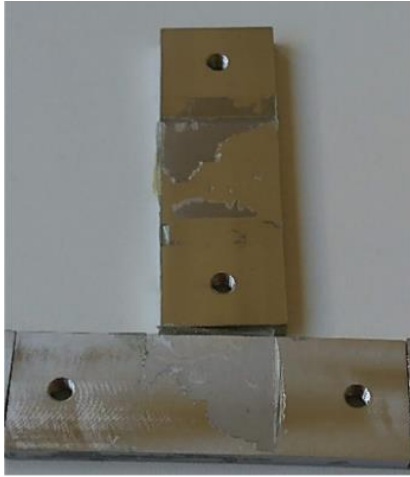
835

836 Figure 4: Effect of carbon chain length in Single Lap Joint (in right with patterns) and Three-
 837 Point Bonding tests (in left in black)



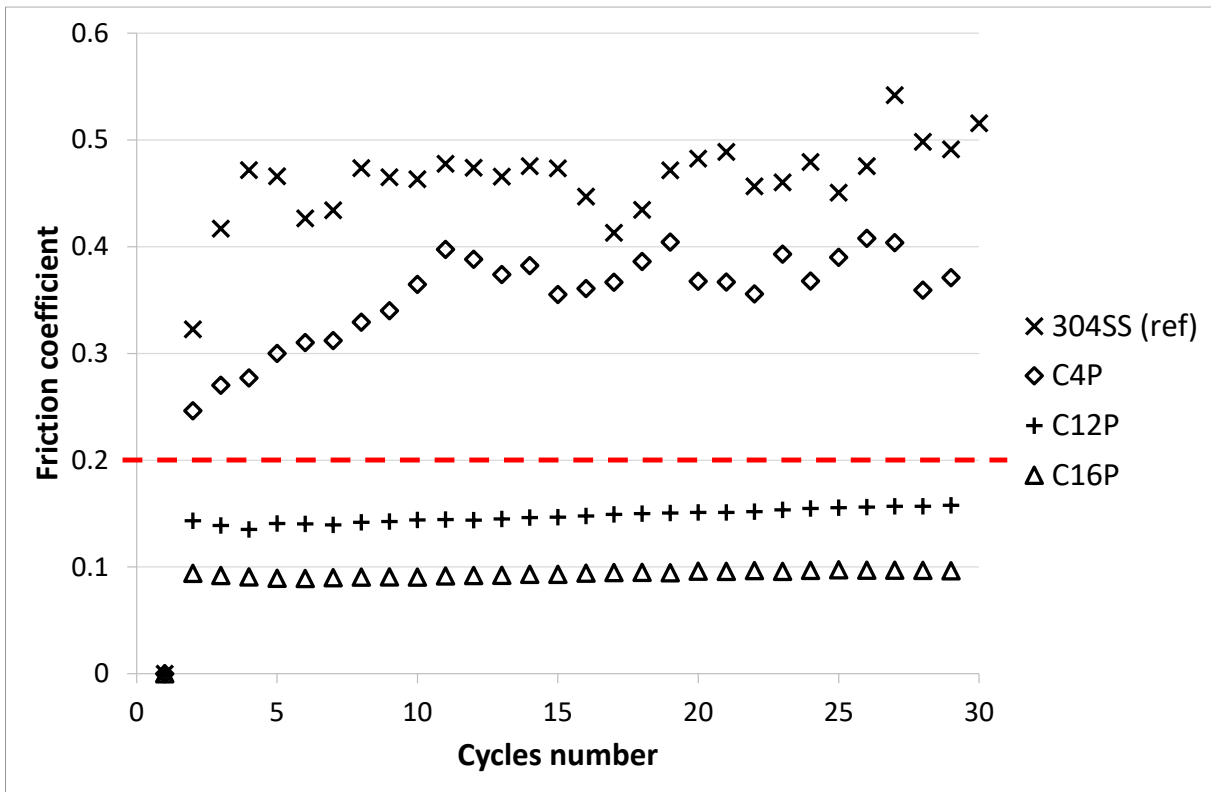
838

839 Figure 5: Schematic illustration of fracture initiation in a three-point bending test



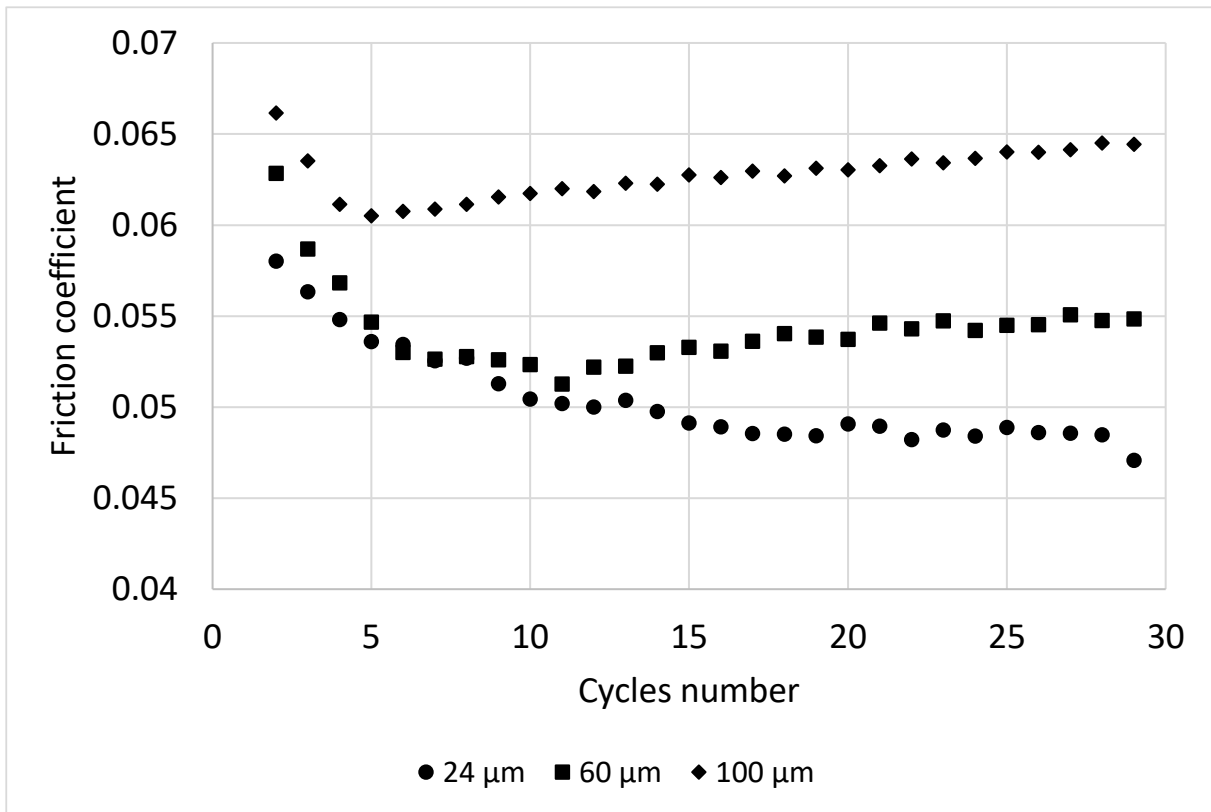
840

841 Figure 6: Single Lap joint (left) and three-point bending (right) samples



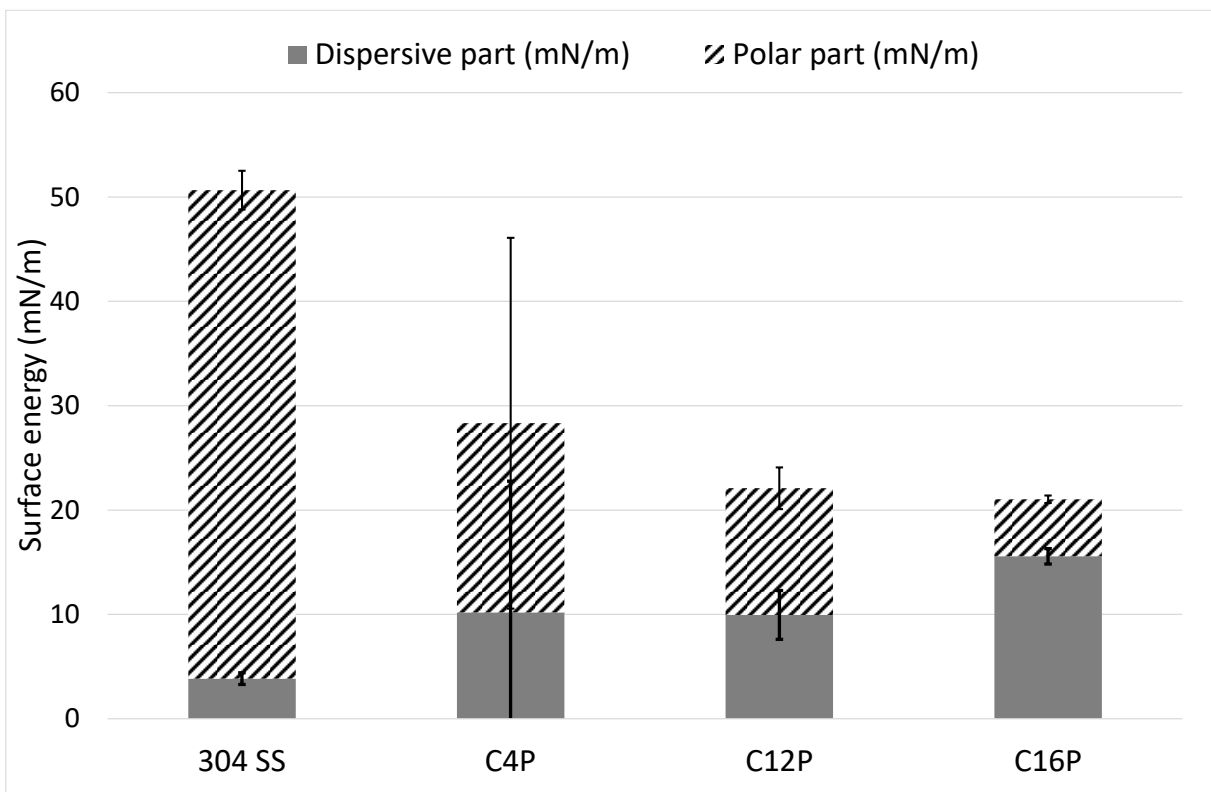
842

843 Figure 7: Friction coefficient of SAMs samples after Three Point Bending tests



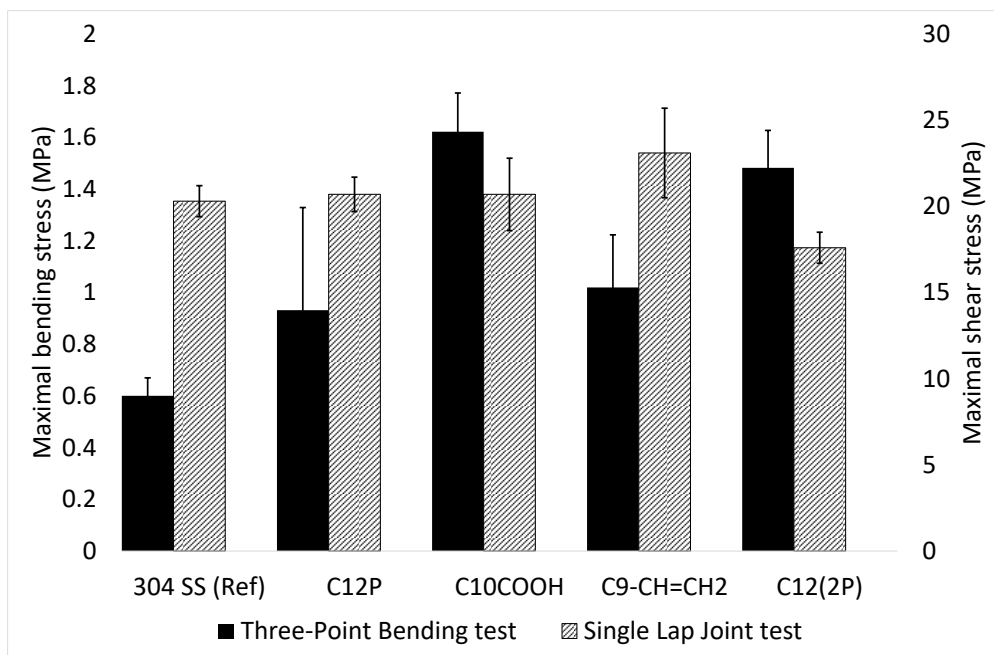
844

845 Figure 8: Friction coefficient as a function of Araldite film thickness



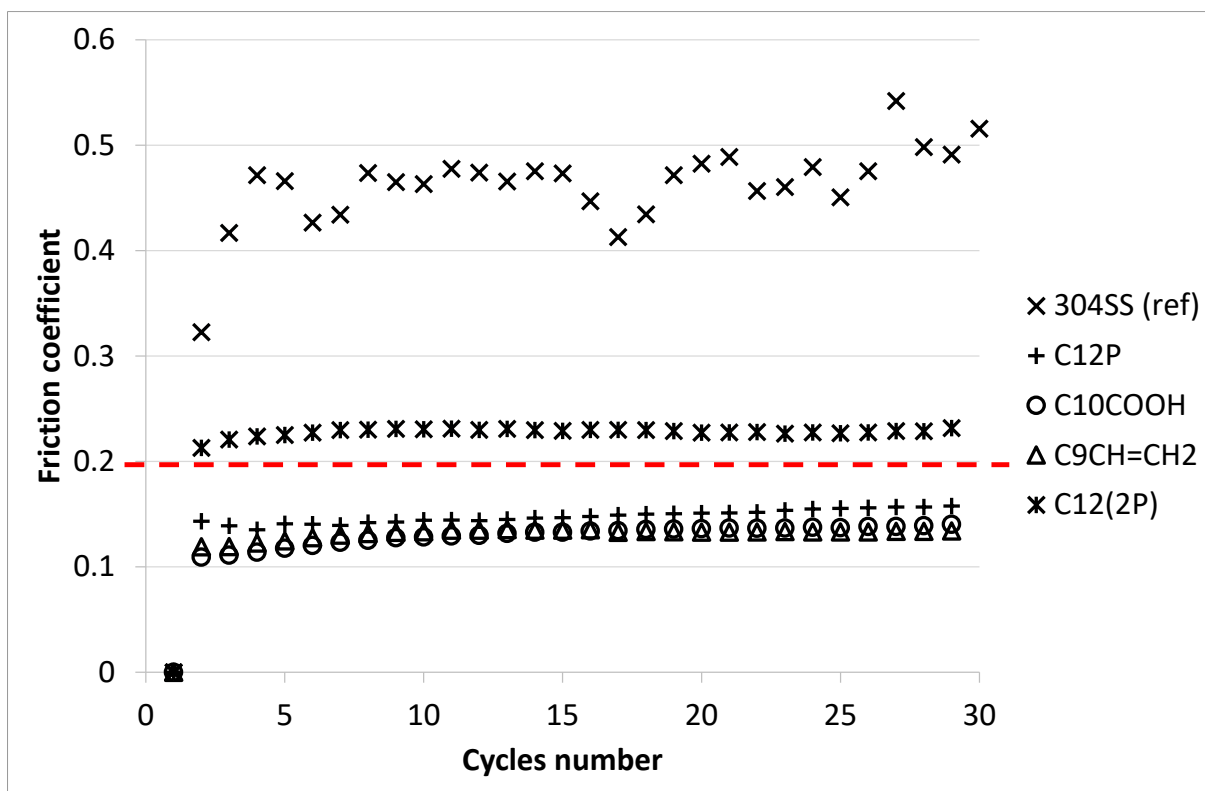
846

847 Figure 9: Surface energy characterization for various length carbon chain



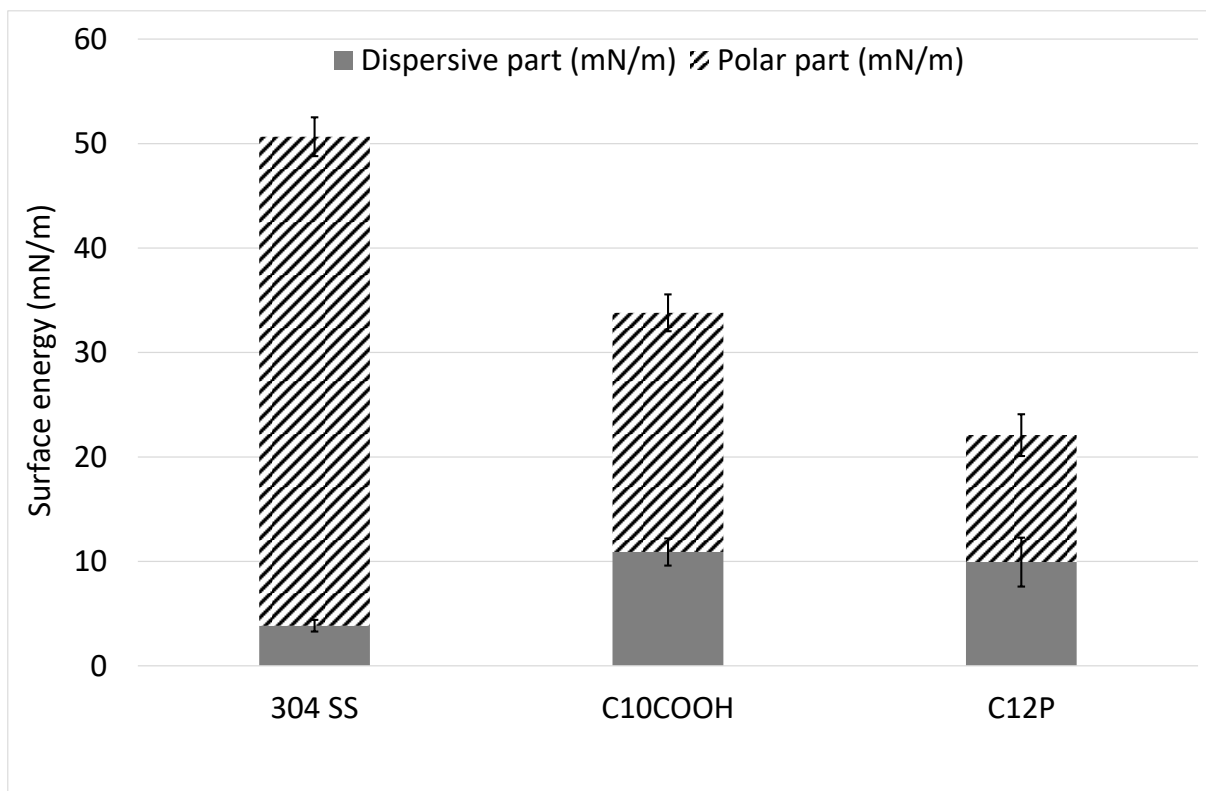
848

849 Figure 10: Effect of terminal group in Single Lap Joint (in right with patterns) and three-point
 850 bending tests (in left in black)



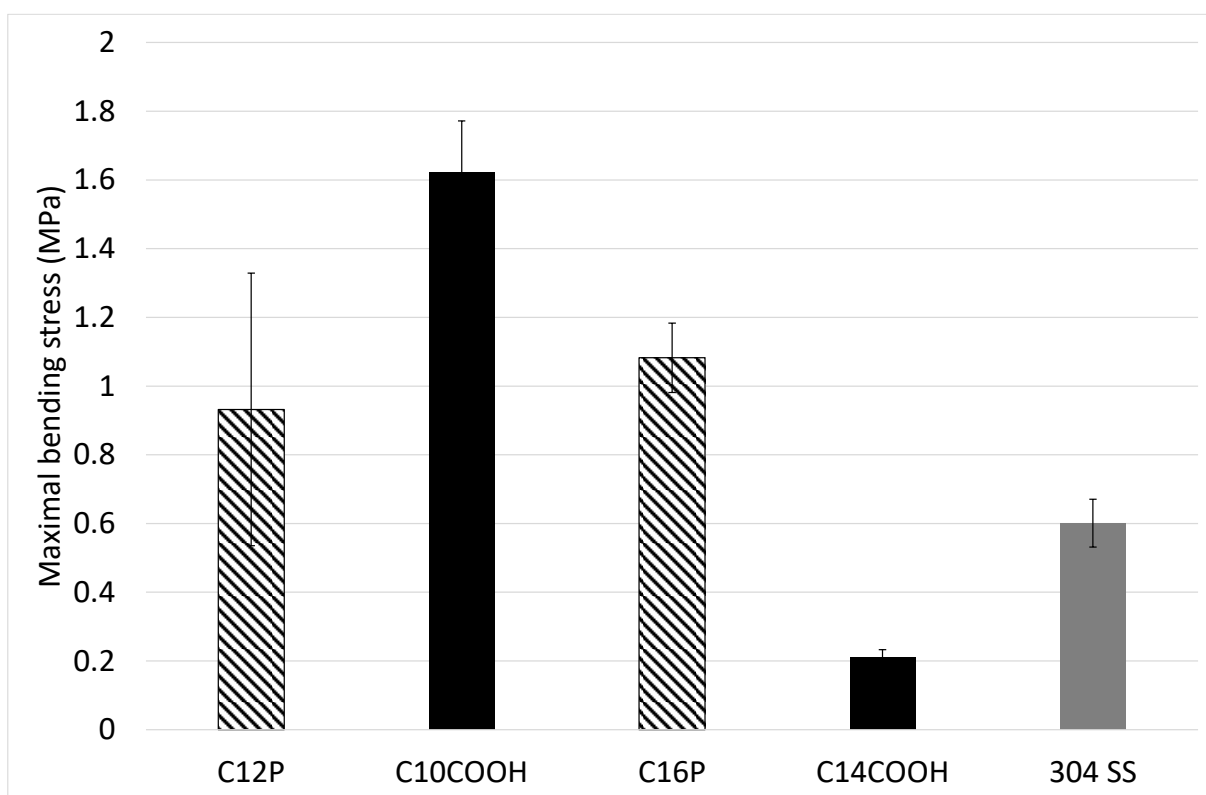
851

852 Figure 11: Friction coefficient of SAMs samples after three-point bending test



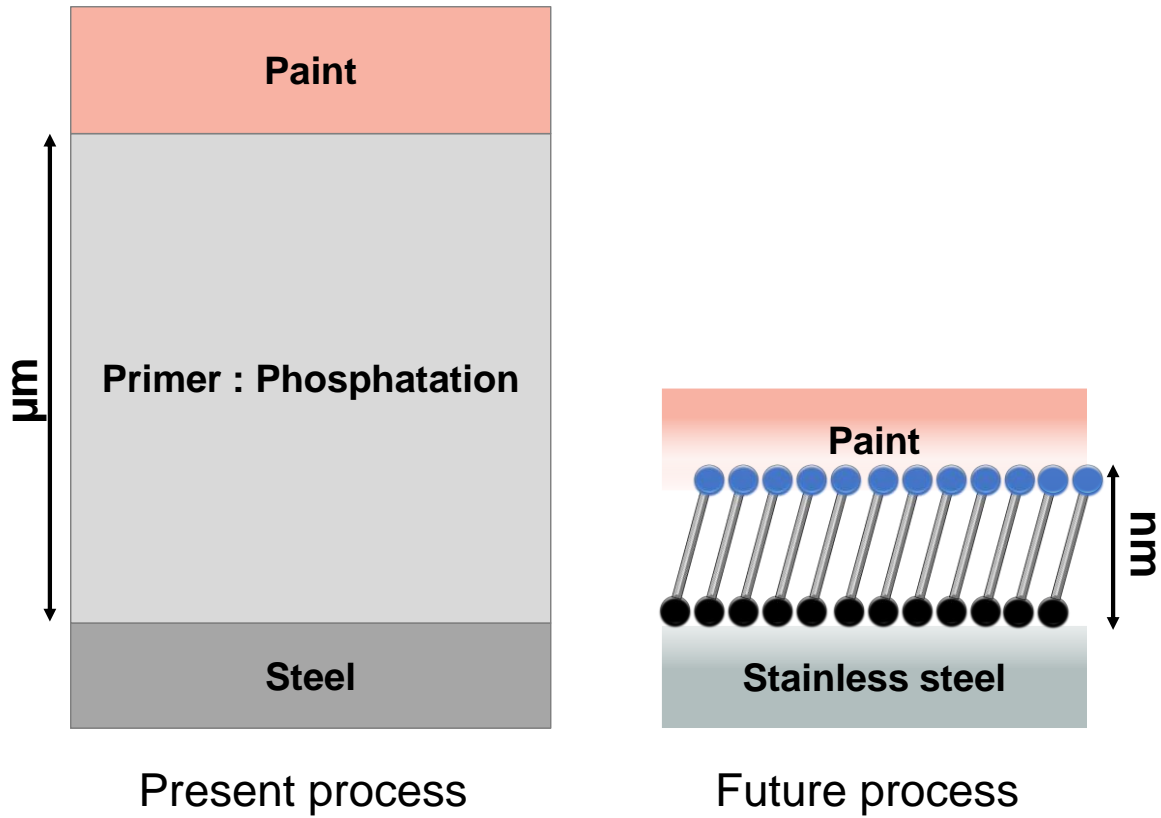
853

854 Figure 12: Surface energy characterization for two terminal groups



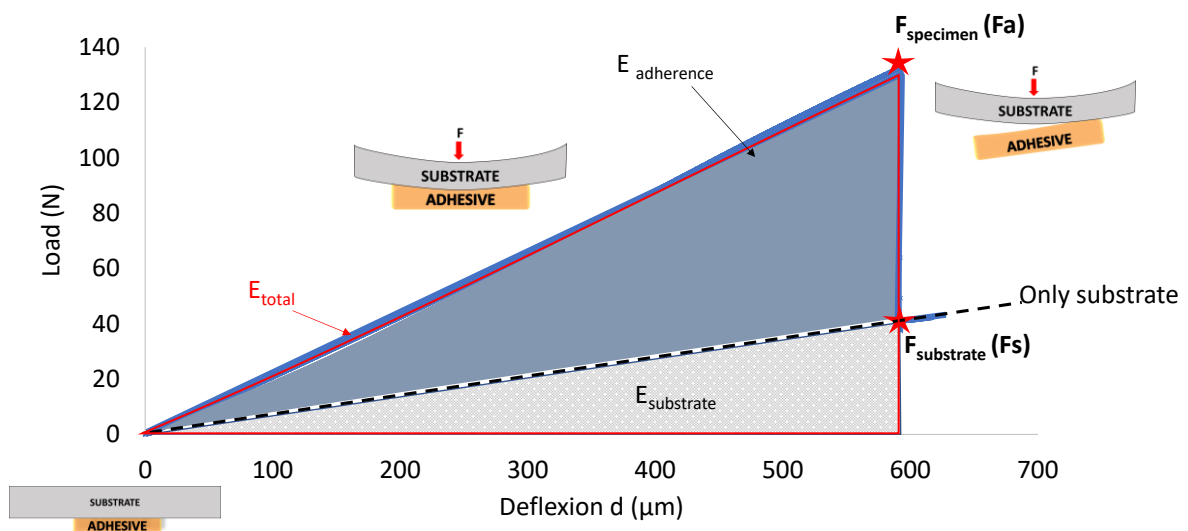
855

856 Figure 13: Effect of terminal group with longer carbon chain in three point Bending test, the
 857 apolar (alkyl) terminations are shown in patterns and the polar (carboxyl) terminations are
 858 represented in black



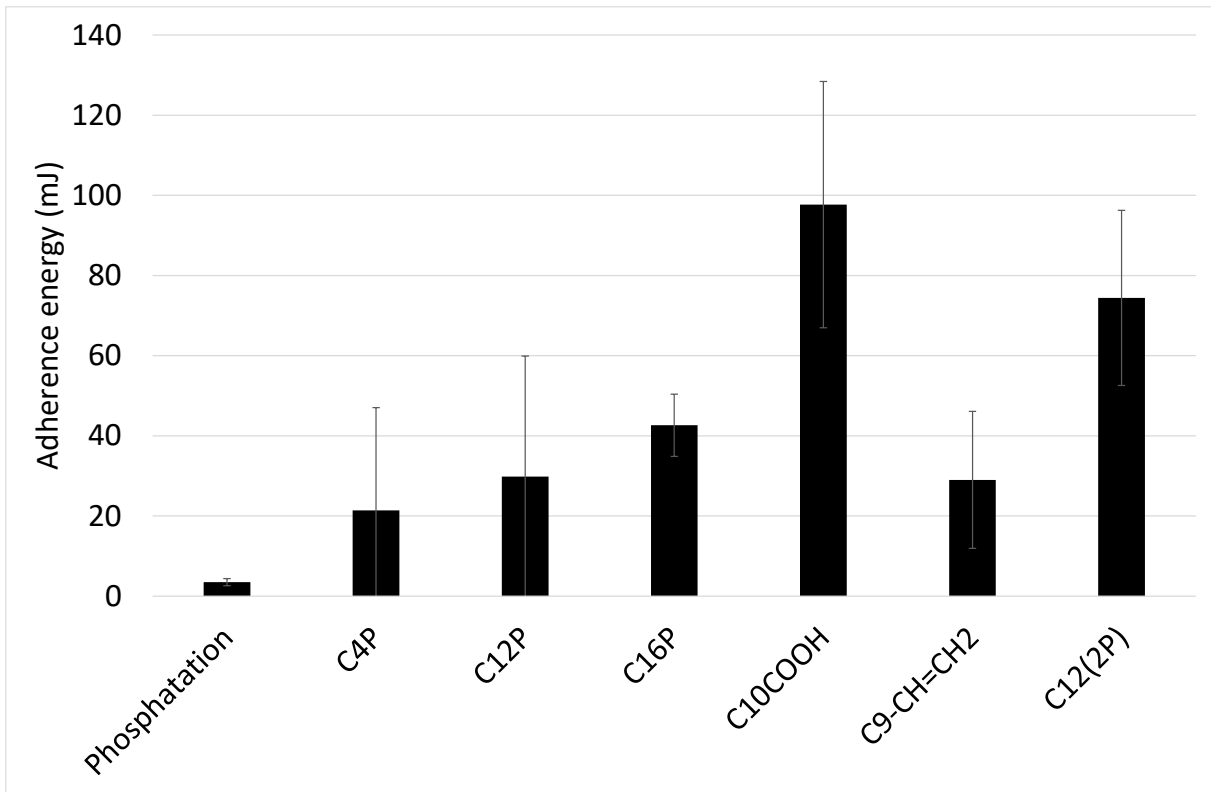
859

860 Figure 14: Schematic representation of the two study systems



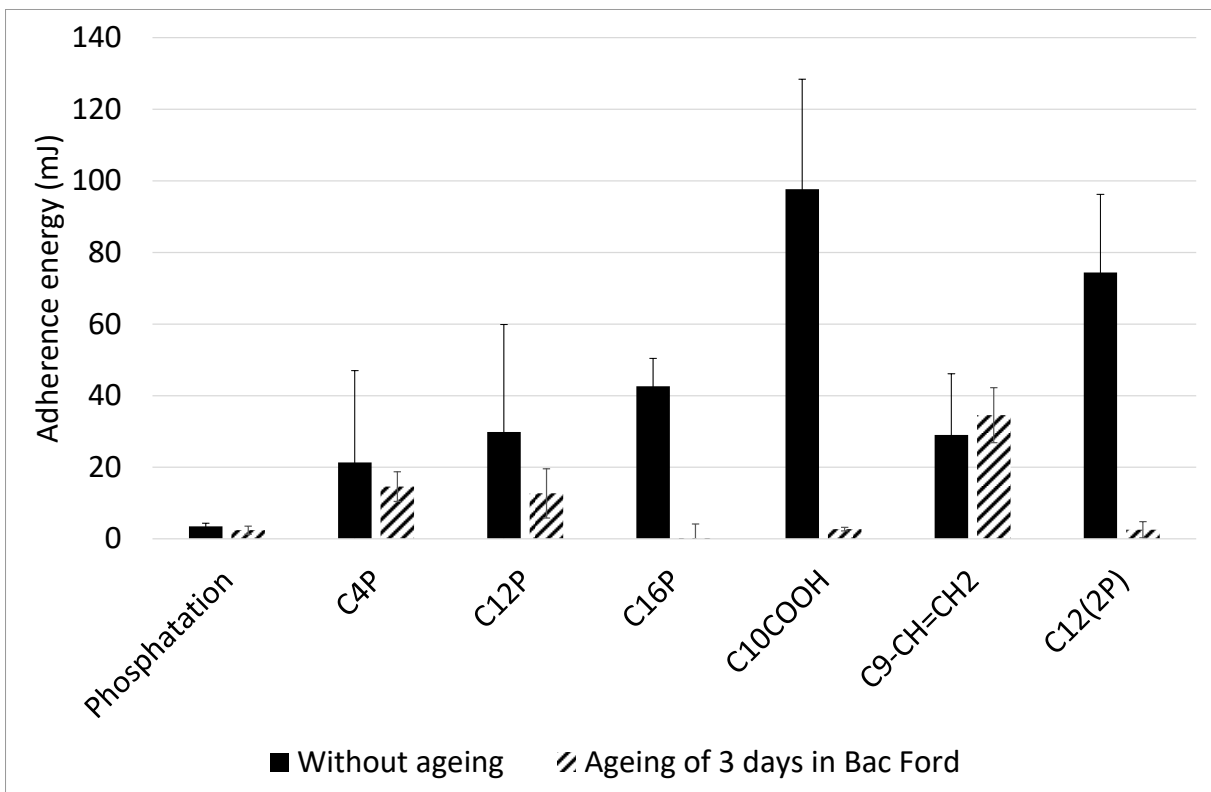
861

862 Figure 15: A typical adherence curve in three-point bending



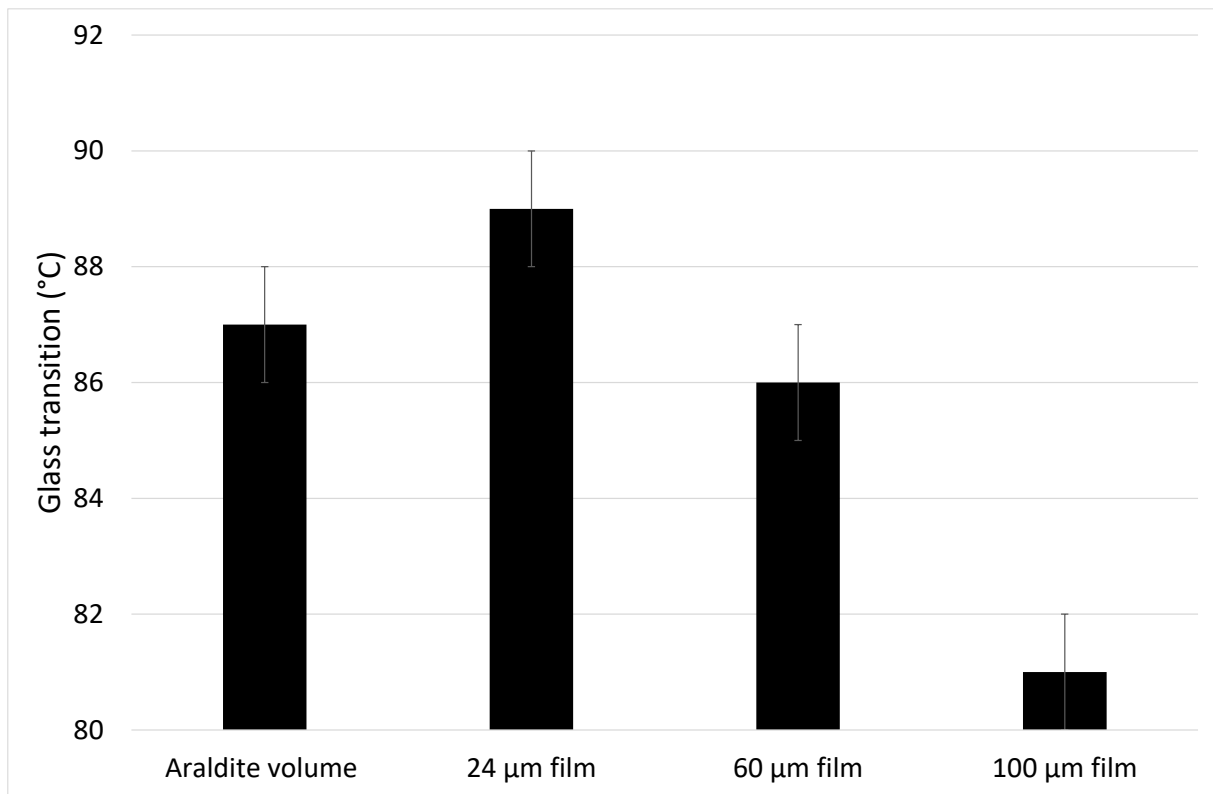
863

864 Figure 16: Adherence energy in three-point bending test



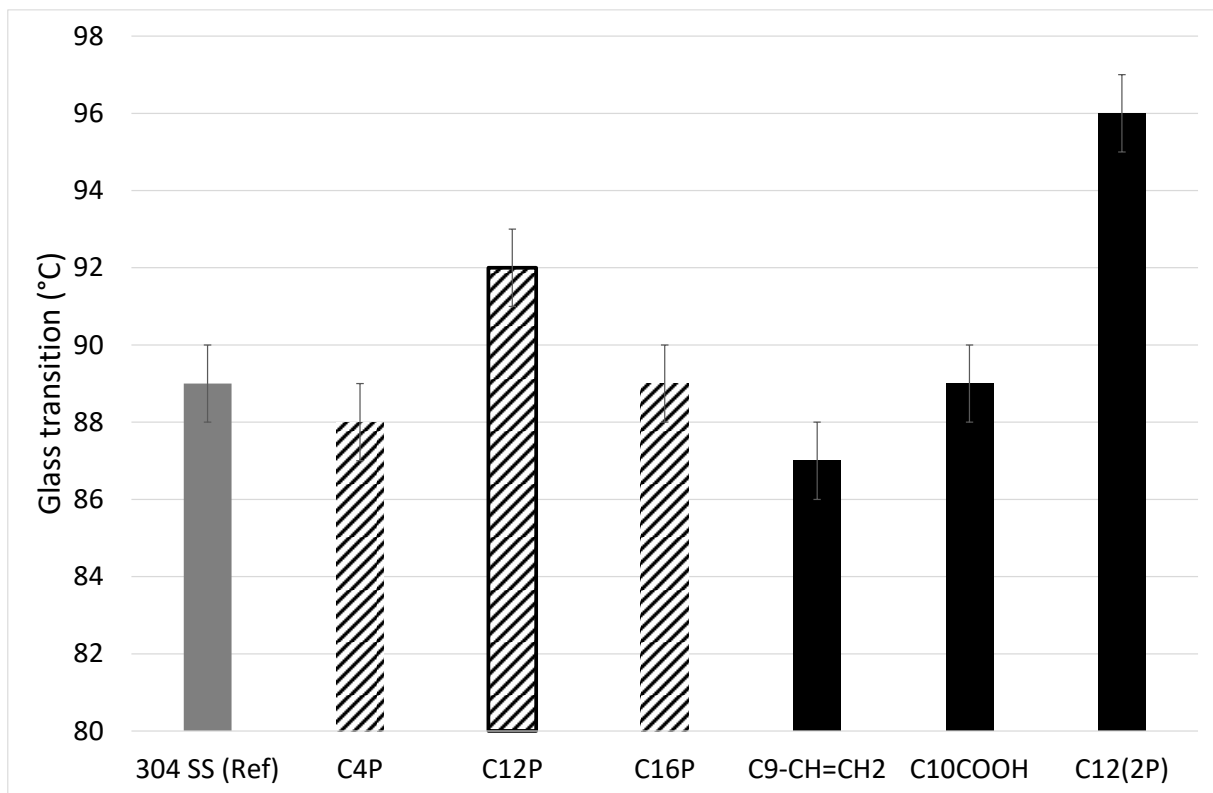
865

866 Figure 17: Impact of ageing in Bac Ford test



867

868 Figure 18: Evolution of the glass transition temperature (onset values) as a function of the
 869 glue thickness on 304SS substrate



870

871 Figure 19: Glass transition according to the tested interphases. The variation of the length of
872 the carbon chain is shown in patterns and the variation of the terminal groups in black. In
873 grey, it's the reference without treatment.

874

875